Journal of Water Process Engineering 52 (2023) 103494

Contents lists available at ScienceDirect

Journal of Water Process Engineering

journal homepage: www.elsevier.com/locate/jwpe

Heterogeneous Fenton- and photo-Fenton-like catalytic degradation of emerging pollutants using Fe_2O_3/TiO_2/pillared clays synthesized from aluminum industrial wastes

Yaneth Cardona [a], Agnieszka Węgrzyn [b], Paweł Miśkowiec [b], Sophia A. Korili [a], Antonio Gil [a,*]

[a] INAMAT^2-Science Department, Los Acebos Building, Public University of Navarra, Campus of Arrosadía, 31006 Pamplona, Spain
[b] Faculty of Chemistry, Jagiellonian University, Gronostajowa 2, 30-387 Kraków, Poland

ARTICLE INFO

Keywords:
Photo-Fenton-like reaction
Alumina-pillared clay
Catalyst
Aluminum saline slag
Organic pollutant

ABSTRACT

The presence of emerging pollutants (EPs) in water is a major environmental concern. This study evaluates for the first time the removal of three EPs, namely triclosan (TCS), 2,6-dichlorophenol (2,6-DCP), and bisphenol A (BPA), 90 μmol/dm^3, from water through both Fenton- and photo-Fenton-like reactions using montmorillonite (Mt) and aluminum interlayered pillared clays (Al-PILC) as catalytic supports. The catalysts (Fe_2O_3/TiO_2/Mt and Fe_2O_3/TiO_2/Al-PILC) were evaluated in single-component solutions and in an equimolar mixture. Two Al-PILC were synthesized from a hazardous waste, namely aluminum saline slag, using either the acid (Al-PILC$_{AE}$) or the alkaline (Al-PILC$_{BE}$) aluminum extract as precursors. The third Al-PILC was obtained by the conventional method using a commercial aluminum salt (Al-PILC$_{CM}$). Catalytic supports were impregnated at 10 and 20 wt% titanium. Iron loadings from 1 to 20 wt% were tested for Mt, while only 20 wt% iron was tested for Al-PILC. All catalysts were characterized using several techniques and the results confirmed the formation of TiO_2 and Fe_2O_3. Almost 100 % of TCS and 2,6-DCP were removed by both Fenton-like (240 and 420 min, respectively) and photo-Fenton-like reactions (30 and 90–120 min, respectively) using the Al-PILC based catalyst. The maximum removal for BPA was 80.14 ± 1.93 % after 120 min under photo-Fenton-like conditions using Al-PILC$_{BE}$. The catalysts synthesized using the four catalytic supports showed good results for the removal of TCS by both processes, while for 2,6-DCP and BPA the best results were obtained using Al-PILC$_{AE}$ and Al-PILC$_{BE}$ as catalytic supports. Finally, a degradation pathway was suggested for every pollutant based on the by-products identified during the reactions by HPLC-MS. The results revealed that the materials used in this work are suitable catalysts for removing emerging pollutants from water by both Fenton- and photo-Fenton-like reactions.

1. Introduction

Water is essential for life and, therefore, the entry of potentially hazardous chemicals into the aquatic environment has always been a major environmental concern [1]. The organic pollutants commonly detected in the environment includes both persistent organic pollutants (POPs) [2] and emerging pollutants (EPs). POPs are considered persistent and extremely toxic, whereas EPs were initially dismissed as eventual pollutants and, as a result, have not been monitored or regulated and thus released into the environment given the lack of information regarding their harmful effects. EPs are all those compounds whose concentration in the environment has increased to the point of generating hazardous effects [3]. Among the list of EPs are triclosan (TCS; 5-chloro-2-(2,4-dichlorophenoxy)phenol), bisphenol A (BPA; 4,4′-(propane-2,2-diyl)diphenol), and 2,6-dichlorophenol (2,6-DCP). TCS is a broad-spectrum antibacterial and preservative agent, which was widely used in many household, personal-care (PCP), and consumer products [1,4–7] but has since been shown to have chronic toxicity and several health effects, including endocrine-disrupting and estrogenic effects [5–8]; BPA, a plasticizer with endocrine-disrupting effects [3,9]; and 2,6-DCP, which, together with TCS, belongs to the chlorophenols (CP) family and is used as an intermediate in several industries and as a raw material for the synthesis of several pharmaceuticals, pesticides, and herbicides. 2,6-DCP has been shown to be highly toxic and harmful to both human health and the environment [10].

Several methods have been studied to remove organic pollutants

* Corresponding author.
E-mail address: andoni@unavarra.es (A. Gil).

https://doi.org/10.1016/j.jwpe.2023.103494
Received 15 October 2022; Received in revised form 22 December 2022; Accepted 6 January 2023
Available online 16 January 2023

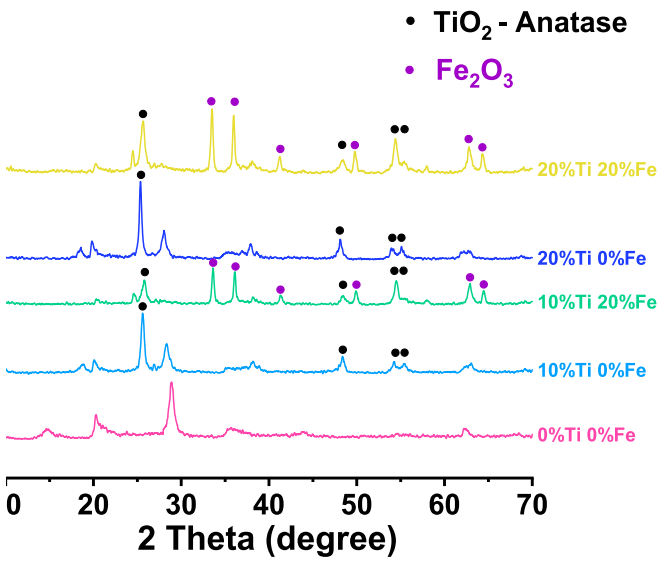

Fig. 1. XRD patterns for Mt, TiO_2/Mt (10 wt% and 20 wt% Ti), and Fe_2O_3/TiO_2/Mt (10 wt% and 20 wt% Ti with 20 wt% Fe).

from water and some conventional methods have exhibited disadvantages, including slow and/or incomplete degradation of the pollutants [11,12]. Advanced oxidation processes (AOPs) have been used and have shown to be an effective alternative for the removal of several toxic, resistant, and stable organic compounds due to their essentially complete lack of selectivity and excellent destructive power [13,14]. AOPs are based on the production and use of hydroxyl radicals (•OH) for oxidation of the target compound [11]. However, the efficiency of the degradation and mineralization can differ between the different AOPs used. These results in the presence of several secondary products formed during the oxidation process in the final solution [11,13]. This means that identification of the by-products formed is essential to ensure that, under the reaction conditions used, this conversion does not generate other hazardous compounds. For example, the chemical structure of TCS is similar to highly toxic and persistent pollutants such as dioxins [1], thus meaning that the formation of dioxins as intermediates during its degradation is possible. In fact, although some studies have reported the effective removal of TCS by photodegradation [7,15], others have identified hazardous by-products such as 2,4-dichlorophenol (2,4-DCP), 2,8-dichlorodibenzo-p-dioxin (2,8-DCDD), and 4,5′-dichloro-2,2′-dihydroxybiphenyl ($(OH)_2$PCB-13), among others [6,8,12,15,16]. These substances have been reported in photocatalytic processes using both solar and UV radiation, as well as in biodegradation studies. 2,8-DCDD, for example, can be converted into higher chlorinated dioxins, which are considered more toxic. This conversion can occur under certain conditions, such as chlorination [6]. This is particularly important given that both UV and chlorine dioxide (ClO_2) are used in water-treatment systems worldwide [16].

The use of various AOPs such as Fenton and photo-Fenton oxidation have been reported for the successful degradation of several organic pollutants [7,11,17,18]. In the Fenton process, the ferrous iron is combined with hydrogen peroxide (Fe^{2+}/H_2O_2) at acidic conditions to generate the hydroxyl radicals (•OH) [19], which degrade the target organic compounds into small organic molecules, which are finally mineralized into CO_2 and H_2O [14,20]. Fenton (Fe^{2+}/H_2O_2) and Fenton-like reactions (Fe^{3+}/H_2O_2) as well as photo-Fenton that use a combination of H_2O_2, Fe(II/III), and light irradiation (UV), have been successfully used to oxidize a wide list of organic pollutants, including chlorinated compounds such as chlorobenzenes, chlorophenols, and chlorinated pesticides, among others [8,11,14,17,21]. The use of solid catalysts in Fenton-like processes to generate the strong oxidants and degrade recalcitrant organic pollutants is also a promising alternative. Several solids have been studied for this purpose, including iron oxide minerals, silicas, zeolites, clays, and pillared clays, among others [22].

The considerable importance of clays as a semiconductor support material lies in their characteristics, including their layered morphology, chemical stability, and cation-exchange ability, as well as their economic advantages and availability [23]. One example of such clays is montmorillonite (Mt), which belongs to the smectite group and is one of the most widely studied and reported in the literature. The use of modified smectites in environmental protection has also been widely documented in the literature [2,24,25]. One of these modification methods consists in introducing pillars between the layers by replacing the exchangeable cations in the clay with rigid metal oxide clusters, thus converting the clays into pillared clays, which have a larger basal spacing and pore volume [26]. Pillared clays have also been successfully studied as catalysts and catalytic supports for several chemical reactions [27–31]. One of the modifications made to catalytic supports for use in catalysis involves the incorporation or deposition of metal and non-metal ions. TiO_2 and Fe^{3+} have been widely used for this purpose due to their characteristics and advantages [13], including the low cost, photostability, non-toxicity, high chemical stability, and catalytic performance [32] However, most of the studies on the use of PILC in catalysis involve Ti-PILC and Fe-PILC, rather than nanocomposites in which the metal is deposited on the PILC using another PILC such as Al-PILC.

Several researchers have used TiO_2/clays and Ti-PILC as photocatalysts for the photodegradation of organic pollutants under both UV or VIS light irradiation in an aqueous suspension. The use of sunlight has also been reported, since this has aroused great interest for the removal of organic pollutants. Dyes are most widely studied pollutants for catalytic photodegradation, being other organic compounds, including herbicides, analgesics, antibiotics and endocrine disruptors have be also considered. Various authors have attempted to modify both TiO_2/clays and Ti-PILC to improve their photocatalytic efficiency under VIS light or sunlight. Indeed, several strategies, such as the use of metal complex ions or photosensitizing dyes, have been applied to photosensitize TiO_2/clays and Ti-PILC. Moreover, modification of the parameters for the deposition methods is also needed, in this case to obtain better nanoparticles and improve their photocatalytic performance. It must always be remembered that PILCs are microporous materials (dp $<$ 2.0 nm) and that organic molecules that degrade should be able to diffuse into their porous structure. Therefore, there is a steric diffusional limitation in this case. In order to broaden the spectrum to other larger pollutant molecules, it would be necessary to increase the structure of the adsorbents synthesized, such as heterostructures or MOF based on clays.

Considering the above, it is vital to explore new alternatives and study new possible catalysts for removing EPs from water. Aluminum pillared clays (Al-PILC) are commonly obtained from commercial chemicals. However, previous studies have shown that those solids synthesized using the remaining aluminum extracted from a hazardous industrial waste (saline slag) are good adsorbents and catalysts for removing EPs from water [32,33]. Repurposing industrial waste to reduce the environmental pollution aligns with the principles of a circular economy. In this case by both turning the hazardous waste into a non-hazardous material and by using it to remove pollutants from water [34]. The use of Al-PILC as catalysts was studied using TiO_2/Al-PILC to photodegrade the EPs. Due to the lack of information about the use of Al-PILC in general as catalytic supports in Fenton and photo-Fenton processes for the removal of EPs this work focuses, for the first time, on the synthesis of both Fe_2O_3/TiO_2/Mt and Fe_2O_3/TiO_2/Al-PILC catalysts by deposition of the metals on the catalytic support, using pillared clays synthesized previously from the aforementioned aluminum saline slags. The catalysts obtained were evaluated for the removal of TCS, BPA, and 2,6-DCP from water by way of Fenton and photo-Fenton reactions in a single component and an equimolar mixture of the three compounds. The by-products formed during the reaction were identified by HPLC-MS, thus allowing us to propose a probable pathway for the

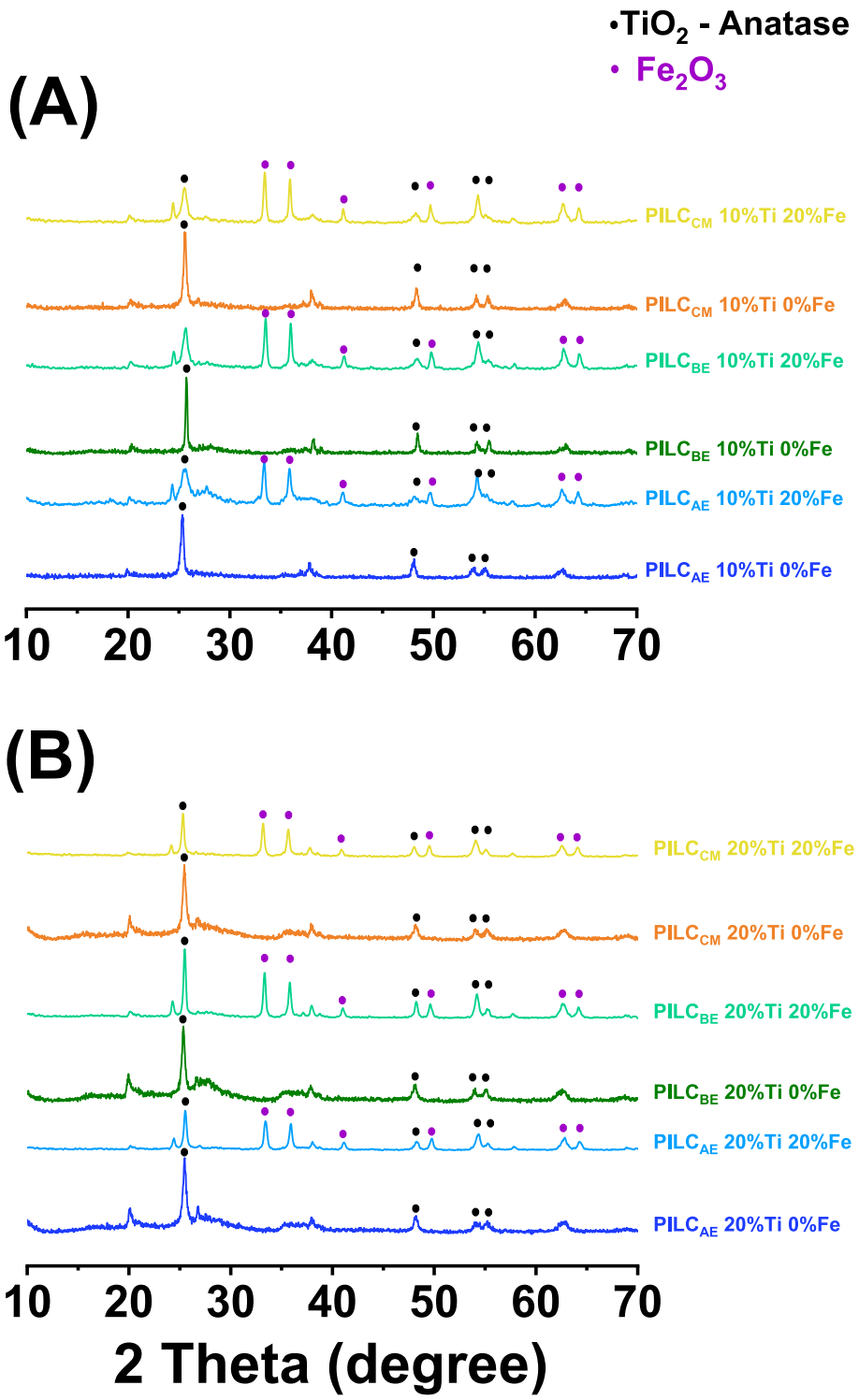

Fig. 2. XRD patterns for TiO_2/Al-PILC (10 wt% and 20 wt% Ti), and Fe_2O_3/TiO_2/Al-PILC (10 wt% and 20 wt% Ti with 20 wt% Fe).

degradation of each of these three pollutants.

2. Experimental procedure

2.1. Materials and reagents

Four catalytic supports with different structural properties [33] were studied in this work, namely, three alumina-pillared clays (Al-PILC) and a montmorillonite (Mt) (supplied by Tsukinuno - The Clay Science Society of Japan), which was the mineral clay used as raw material in the synthesis of all three Al-PILC. The difference between the three Al-PILC was the aluminum source in the intercalation solution used in their synthesis. Thus, one of them (Al-$PILC_{CM}$) was prepared using the conventional aluminum source (an aluminum salt) in the intercalation solution, whereas the other two were synthesized using the aluminum extracted from a hazardous waste produced in the secondary aluminum production process, known as saline slags. In this case, the difference was that one of them used the alkaline extract (Al-$PILC_{BE}$) and the other

Table 1
Specific surface area (S_{BET}), total pore volume (V_{Total}), and average pore diameter (dp) for all the Fe_2O_3-TiO_2 catalysts.

Catalyst support	wt% titanium	wt% iron	S_{BET} (m^2/g) - mean ± SD	V_{Total} (cm^3/g) - mean ± SD	dp (nm) - mean ± SD
Mt	0	0	10 ± 1	0.05 ± 0.01	19.4 ± 0.3
	10	0	32 ± 4	0.07 ± 0.02	8.5 ± 2.0
		1	32 ± 1	0.08 ± 0.01	9.5 ± 1.5
		5	30 ± 1	0.05 ± 0.01	7.0 ± 1.0
		10	28 ± 3	0.05 ± 0.01	7.6 ± 1.1
		20	25 ± 1	0.05 ± 0.01	8.7 ± 0.39
	20	0	29 ± 5	0.07 ± 0.01	9.8 ± 1.0
		1	32 ± 1	0.07 ± 0.01	9.1 ± 1.3
		5	35 ± 3	0.08 ± 0.01	9.5 ± 1.5
		10	46 ± 3	0.12 ± 0.02	10.0 ± 2.2
		20	52 ± 5	0.10 ± 0.02	7.9 ± 1.8
Al-$PILC_{CM}$	0	0	173 ± 14	0.15 ± 0.01	3.5 ± 0.3
	10	0	138 ± 5	0.10 ± 0.02	4.0 ± 1.0
		20	69 ± 5	0.10 ± 0.02	5.7 ± 1.3
	20	0	78 ± 3	0.08 ± 0.01	5.0 ± 1.0
		20	60 ± 6	0.11 ± 0.01	7.0 ± 0.3
Al-$PILC_{BE}$	0	0	124 ± 6	0.11 ± 0.01	4.3 ± 0.5
	10	0	82 ± 8	0.06 ± 0.03	5.0 ± 0.3
		20	60 ± 8	0.11 ± 0.01	7.4 ± 1.1
	20	0	59 ± 4	0.04 ± 0.01	6.0 ± 0.4
		20	46 ± 6	0.10 ± 0.03	8.4 ± 1.0
Al-$PILC_{AE}$	0	0	277 ± 10	0.21 ± 0.01	3.0 ± 0.1
	10	0	193 ± 14	0.11 ± 0.03	4.5 ± 0.4
		20	87 ± 9	0.10 ± 0.01	4.8 ± 0.8
	20	0	83 ± 9	0.09 ± 0.01	4.5 ± 0.1
		20	75 ± 3	0.08 ± 0.01	4.4 ± 0.5

the acid one (Al-$PILC_{AE}$). The chemical composition by FRX of the saline slags is: Na_2O (8.65 wt%), MgO (2.76 wt%), Al_2O_3 (41.71 wt%), SiO_2 (4.23 wt%), P_2O_5 (0.05 wt%), Cl (11.83 wt%), K_2O (4.40 wt%), CaO (2.08 wt%), TiO_2 (0.31 wt%), Cr (0.04 wt%), MnO (0.17 wt%), Fe_2O_3 (2.05 wt%), Cu (0.35 wt%), F (0.41 wt%), Zn (0.18, wt%).

The three organic pollutants studied were 2,6-dichlorophenol (2,6-DCP; $C_6H_4Cl_2O$ - Acros Organics), triclosan (TCS; $C_{12}H_7Cl_3O_2$ - Ambeed), and bisphenol A (BPA; $C_{15}H_{16}O_2$ - Acros Organics). Methanol (ChemSolve) was used during the preparation of their aqueous solutions to enhance their solubility, and hydrochloric acid (37 %, PanReac AppliChem) to adjust the solution pH.

Titanium(IV) isopropoxide (>97 %, Sigma-Aldrich), iron(III) nitrate nonahydrate (PanReac AppliChem), HCl (37 %, PanReac AppliChem), and isopropyl alcohol (>99 %, Sigma-Aldrich) were used during impregnation of the catalytic supports. HPLC-grade acetonitrile (ACN – J.T Baker) and formic acid (Sigma-Aldrich) were used for the high-performance liquid chromatography (HPLC) analysis, to quantify the three pollutants in the experiments, and to identify their by-products. Hydrogen peroxide (H_2O_2 - ChemPur) was used in both Fenton-like and photo-Fenton-like experiments.

2.2. Synthesis of the catalysts

The catalytic supports used in this work were montmorillonite (Mt - supplied by Tsukinuno - The Clay Science Society of Japan) and three aluminum-pillared clays (Al-$PILC_{CM}$, Al-$PILC_{BE}$, and Al-$PILC_{AE}$) synthesized using the Mt as the raw clay. Al-$PILC_{CM}$ was synthesized using the conventional method, using commercial aluminum chloride ($AlCl_3{\cdot}6H_2O$) and NaOH in a hydrolysis reaction (OH^-/Al^{3+}) of 2.0 for the preparation of the intercalation solution. Al-$PILC_{BE}$ and Al-$PILC_{AE}$ were synthesized using the aluminum extracted from the saline slag by the alkaline or acid extraction method, respectively.

The synthesis and characterization of the three Al-PILC is explained in a previous work [33]. The mentioned work evaluated the parameters to prepare the intercalating solution that allows the synthesis of Al-PILC with the highest textural properties using aluminum extracts. The

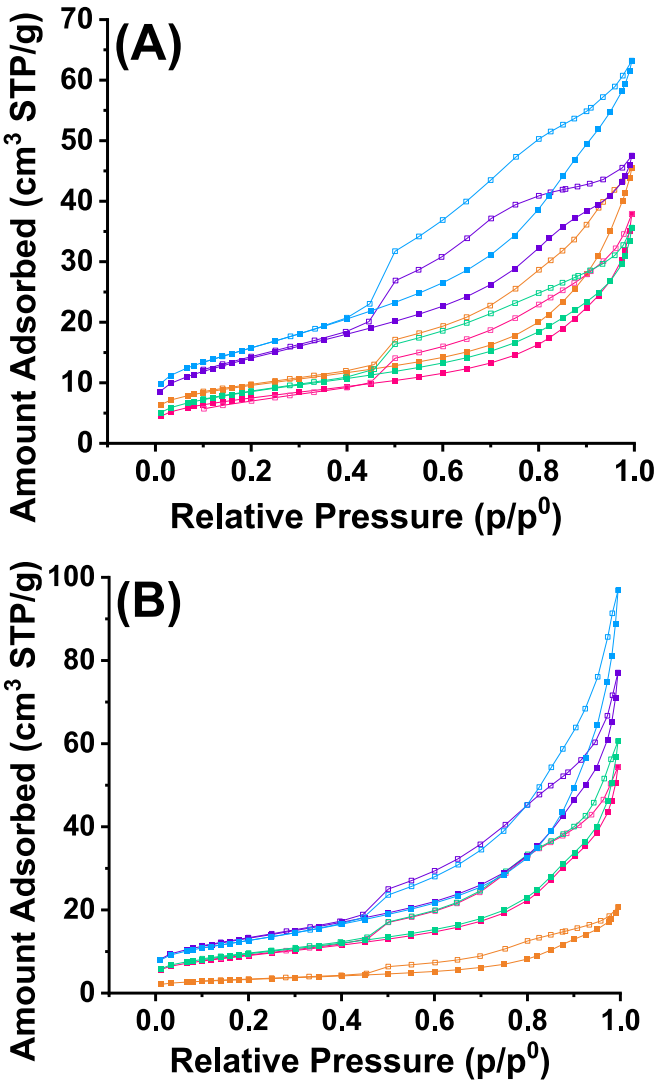

Fig. 3. N_2 adsorption (square solid) and desorption (square hollow) results at −196 °C for TiO_2/Mt and Fe_2O_3/TiO_2/Mt containing (A) 10 wt% Ti, and (B) 20 wt% Ti, with various Fe contents (wt%): 0 (orange), 1 (pink), 5 (green), 10 (purple), and 20 (blue). (For interpretation of the references to colour in this figure legend, the reader is referred to the web version of this article.)

parameters used for the preparation of the intercalating solution differ for the aluminum extracts (alkaline and acid). The $[OH^-]/[Al^{3+}]$ molar ratio was 2.0 for both, however, the Al/clay (mmol/g) ratio was 20.0 (Alkaline) and 7.0 (Acid), and the Clay/volume solution ratio was 8.0 (Alkaline) and 6.0 (Acid). In the case of the alkaline extract, the pillaring solution was prepared at room temperature (24 °C) and the acidic extract at high temperature (>90 °C). The pH of the pillaring solutions was around 3.9–4.2. Both titration and aging time was 1 h and the intercalation time was 22 h at room temperature. At the end of the intercalation process, the intercalated clays were separated from the solution by centrifugation (Hettich ROTANTA 460 S) and washed several times with distilled water. Then, they were dried (100 °C for 8 h) and subsequently calcinated (500 °C for 4 h, 1 °C/min) in an oven (Nabertherm L5/S27) to produce the Al-PILC.

All four catalytic supports studied (Al-$PILC_{CM}$, Al-$PILC_{BE}$, Al-$PILC_{AE}$, and Mt) were dried at 150 °C for 12 h. Modification of these supports was carried out by first including the titanium, to obtain TiO_2/Mt and TiO_2/Al-PILC, and then the iron, to obtain Fe_2O_3/TiO_2/Mt and Fe_2O_3/TiO_2/Al-PILC. Both these modifications (iron and titanium) were carried out using a well-known method, namely impregnation through stirring

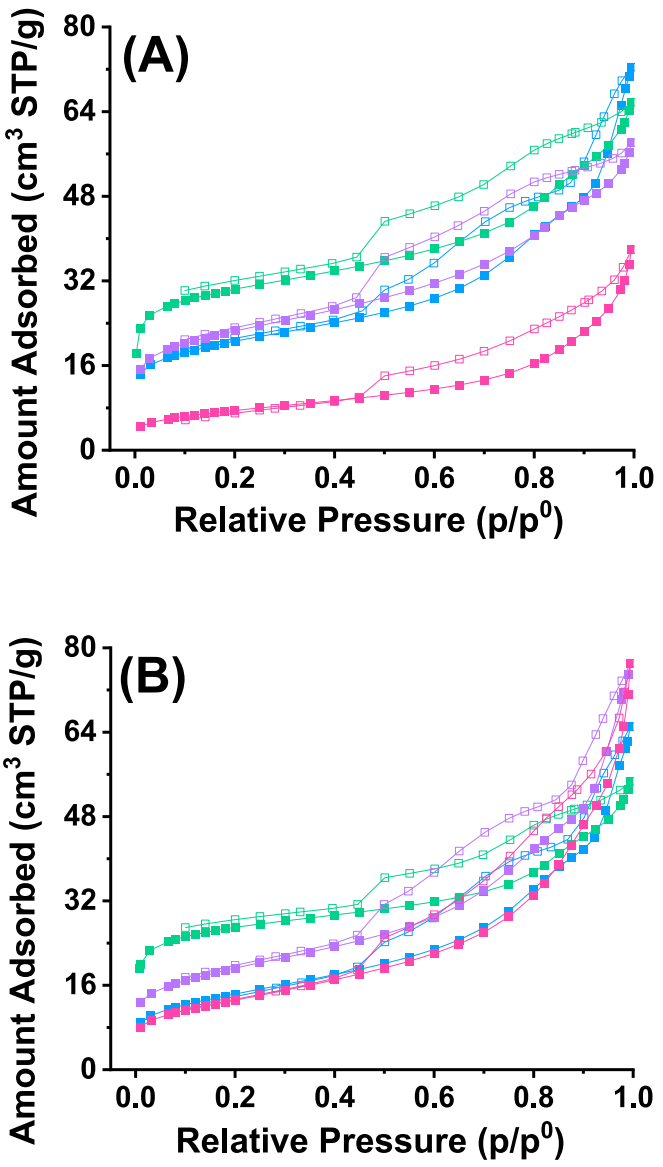

Fig. 4. N_2 adsorption (square solid) and desorption (square hollow) results at −196 °C for the Fe_2O_3/TiO_2/Mt and Al-PILC catalysts containing (A) 10 wt% Ti with 20 wt% Fe, and (B) 20 wt% Ti with 20 wt% Fe, using Mt (pink), $PILC_{CM}$ (purple), $PILC_{AE}$ (green), and $PILC_{BE}$ (blue) as catalytic supports. (For interpretation of the references to colour in this figure legend, the reader is referred to the web version of this article.)

followed by calcination [35].

The appropriate amount of the respective impregnating agent was calculated by taking into account the desired percentage of each in the catalyst. In the light of preliminary results, all four catalytic supports were modified using two mass percentages of Ti (10 and 20 wt%). Mt doped at both titanium mass percentages (10 and 20 wt%) was impregnated with four loadings of iron (1, 5, 10, and 20 wt%) and evaluated as catalytic support in the Fenton-like reaction. In view of the results obtained, all three Al-PILC studied in this work, at both titanium mass percentages (10 and 20 wt%), were impregnated with iron only at the highest iron mass percentage (20 wt%). Both values used in the impregnation steps agree with values previously used by other authors [36,37].

In a few cases, especially for the lower metal content, the desired metal loading was added in a single step. However, in others, especially for the higher metal contents, successive impregnations were required because the volume of the solutions needed was higher than the water pore-volume of the catalytic supports. Between these impregnation steps, the loaded catalytic supports were dried at 100 °C for 3 h to remove the solvent. At the end of the impregnation procedure, once the desired amount had been impregnated into the catalytic supports, they were dried at 100 °C for 8 h and 150 °C for 12 h. Finally, the dried solids were calcined at 500 °C for 4 h (1 °C/min).

2.3. Characterization techniques

The textural properties of the catalysts studied in this work were analyzed using N_2 (Praxair, 99.999 %) adsorption experiments at −196 °C using a gas sorption analyzer (Micromeritics model ASAP 2020 Plus). Samples (0.2 g) were degassed prior to the analysis (200 °C for 12 h) at a pressure lower than 0.1 Pa. The total pore volume (V_{Total}) was calculated using the amount of nitrogen adsorbed at a relative pressure of 0.98, and the specific surface area (S_{BET}) of the catalysts in the relative-pressure range from 0.05 to 0.2 was estimated using the Brunauer-Emmett-Teller (BET) method. The catalysts were characterized by powder X-ray diffraction (XRD) using a BRUKER D-8 ADVANCE eco X-ray diffractometer. Ni-filtered Cu Kα radiation (λ = 0.1548 nm) was used, operating in the range from 8° to 70° (2θ) at a scan rate of 0.2° (2θ)/min. Finally, the morphology and the chemical composition of the catalysts were determined by scanning electron microscopy (SEM), energy-dispersive X-ray spectrometry (INSPECT- F50 at 10 kV), and transmission electron microscopy (TEM) using a Tecnai T30 transmission electron microscope operating at an accelerating voltage of 200 kV.

2.4. Fenton and photo-Fenton-like reactions

Aqueous solutions of each pollutant (90 μmol/dm^3) were prepared, and their pH was adjusted to 3.5 using HCl (aq). This pH value was chosen as is it well known that both Fenton and Fenton-like reactions are more effective under acidic conditions [13,38,39]. The solution of the respective pollutant (15 cm^3) at that pH value was mixed in a round bottom glass reactor with the respective catalyst (15 mg), and magnetically stirred continuously in the dark (700 rpm) for 15 min to establish the adsorption-desorption equilibrium between the pollutants and the catalyst surface. At this point, the respective Fenton or photo-Fenton catalytic test was started, adding the oxidant (H_2O_2) at a molar ratio of 1:10 with respect to the pollutant. The molar ratio of H_2O_2 was calculated using the theoretical stoichiometric amount required for complete oxidation of the three pollutants. This value was chosen based on the results obtained in preliminary experiments. In the case of photo-Fenton experiments, the reaction was carried out in a UV reactor equipped with 20 monochrome Hg lamps (power 160 W) with a continuous UV-A radiation spectrum with mean peaks at 350 nm. In photo-Fenton experiments, once the H_2O_2 had been added, the UV source was turned on to allow the reaction to occur under exposure to UV radiation.

Once the Fenton or photo-Fenton reaction had started, aliquots were taken from the suspension at established time intervals. These aliquots were centrifuged at 6000 rpm (IFUGE M08 - Microcentrifuge from Neuation) and filtered (hydrophilic PTFE, diameter 1.3 cm, pore diameter 0.22 μm) to ensure complete removal of the catalyst. The conversion efficiency was determined by HPLC-MS, measuring the amount of pollutant eliminated from the solution after those given periods of time. All experiments were repeated once.

In addition to the single component solutions, an equimolar aqueous solution of the three pollutants at 90 μmol pollutant/dm^3 was prepared to study the Fenton and photo-Fenton catalytic degradation of this mixture. The pH of the solution was adjusted to 3.5 using HCl (aq), and the Fenton and photo-Fenton procedures were carried out as described for the single-component solutions. The percentage of pollutant adsorbed, the percentage of pollutant converted, and the percentage of pollutant removed were determined by calculating the difference

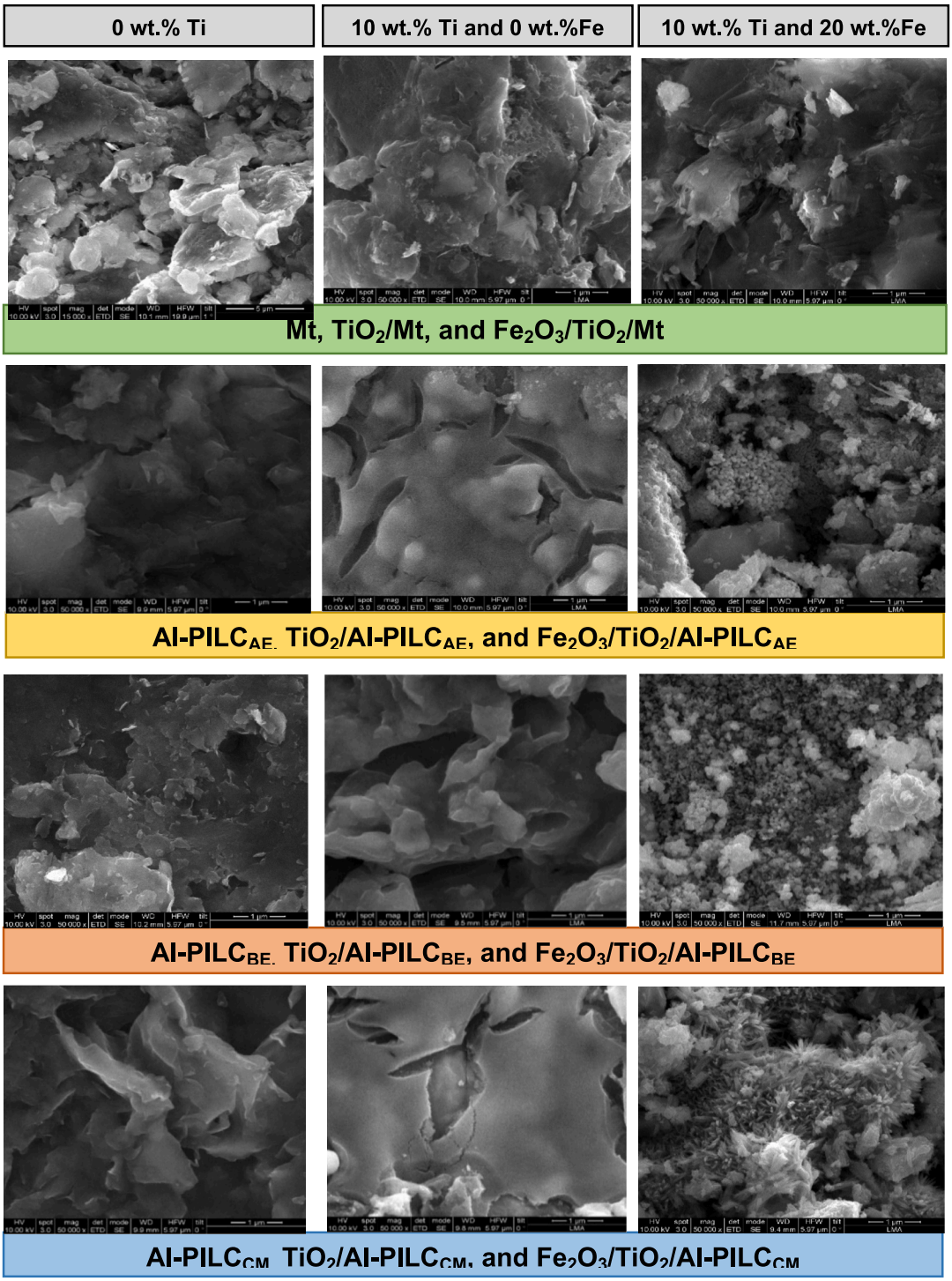

Fig. 5. SEM images for Mt, Al-PILC$_{AE}$, Al-PILC$_{BE}$, and Al-PILC$_{CM}$ used as catalytic supports and the catalysts at 20 wt% Ti and 0 wt% Fe, and 20 wt% Ti and 20 wt% Fe at 50,000× Magnification.

between the initial and remaining concentrations using Eqs. (1)–(3):

$$Pollutant\ Adsorbed\ (\%) = \frac{C_0 - C_{t1}}{C_0} \times 100 \quad (1)$$

$$Pollutant\ Converted(\%) = \frac{C_{t1} - C_{t2}}{C_{t1}} \times 100 \quad (2)$$

$$Pollutant\ Removed\ (\%) = \frac{C_0 - C_{t2}}{C_0} \times 100 \quad (3)$$

where C_0 (μmol/dm^3), C_{t1} (μmol/dm^3) and C_{t2} (μmol/dm^3) correspond to the initial concentration of the organic compound at the beginning of the experiment (90 μmol/dm^3), the concentration of organic compound at 15 min, when the dark adsorption period finished and the Fenton and photo-Fenton experiments started, and, finally, the concentration of the organic pollutant at the respective sampling time, which for calculation of the final value was the concentration of pollutant in the final sampling, at the end of the experiment.

The kinetics for oxidation of the organic pollutants by both Fenton

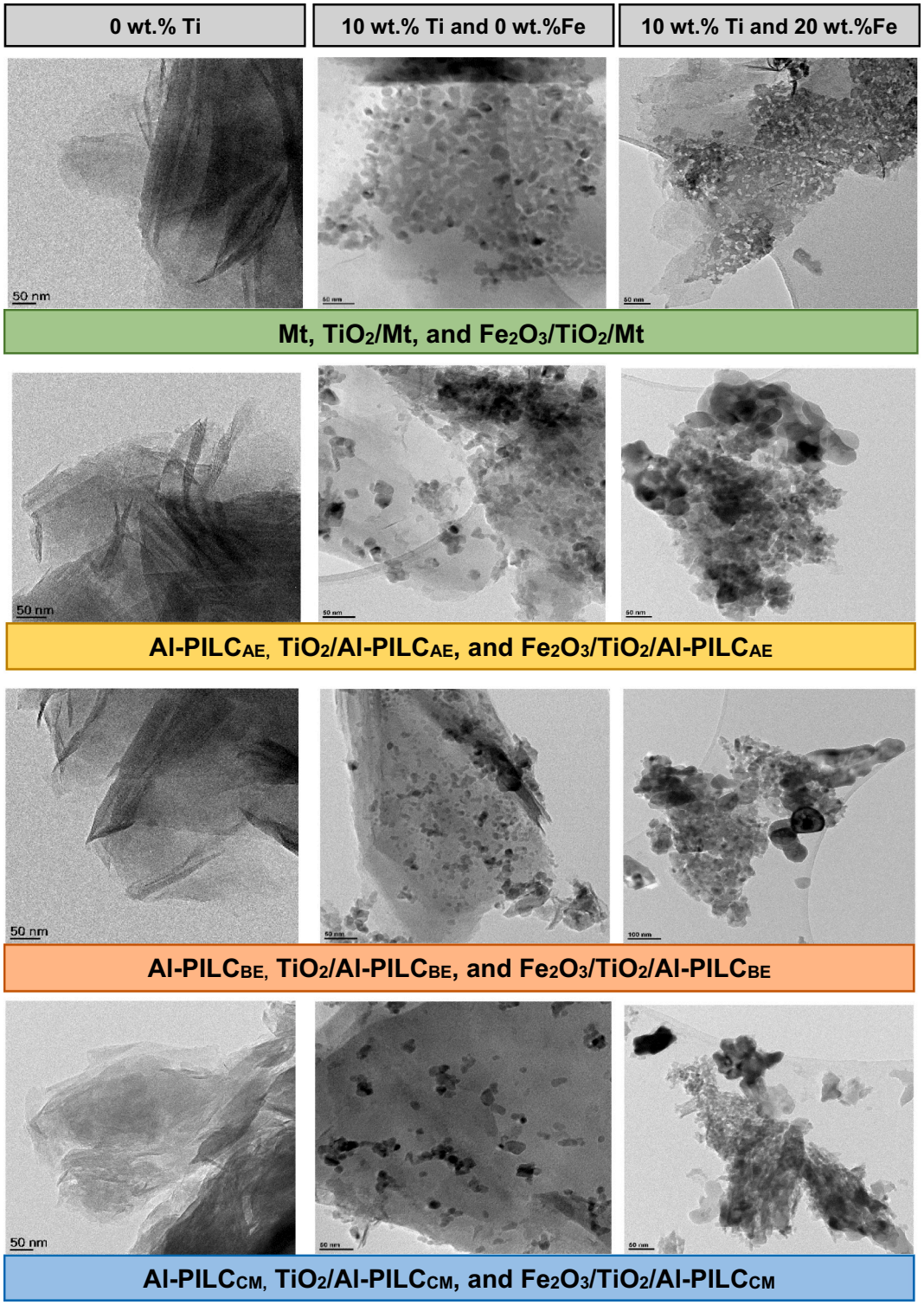

Fig. 6. TEM images for Mt, Al-PILC$_{AE}$, Al-PILC$_{BE}$, and Al-PILC$_{CM}$ used as catalytic supports and the catalysts at 20 wt% Ti and 0 wt% Fe, and 20 wt% Ti and 20 wt % Fe.

and photo-Fenton processes can be represented as follows:

$$\frac{dC_p}{dt} = -k_p C_p C_{\cdot OH} \tag{4}$$

where C_p and $C_{\cdot OH}$ are the concentrations (μmol/dm^3) of pollutant and hydroxyl radical, and k_p is the rate constant for the reaction. Under certain reaction conditions, the concentration of hydroxyl radical is constant [40], thus leading to the following reduced pseudo-first-order equation:

$$\frac{dC_p}{dt} = -k_1 C_p \tag{5}$$

where k_1 is the pseudo-first-order rate constant. When $t = 0$, C_p is equal to C_{p0}, then:

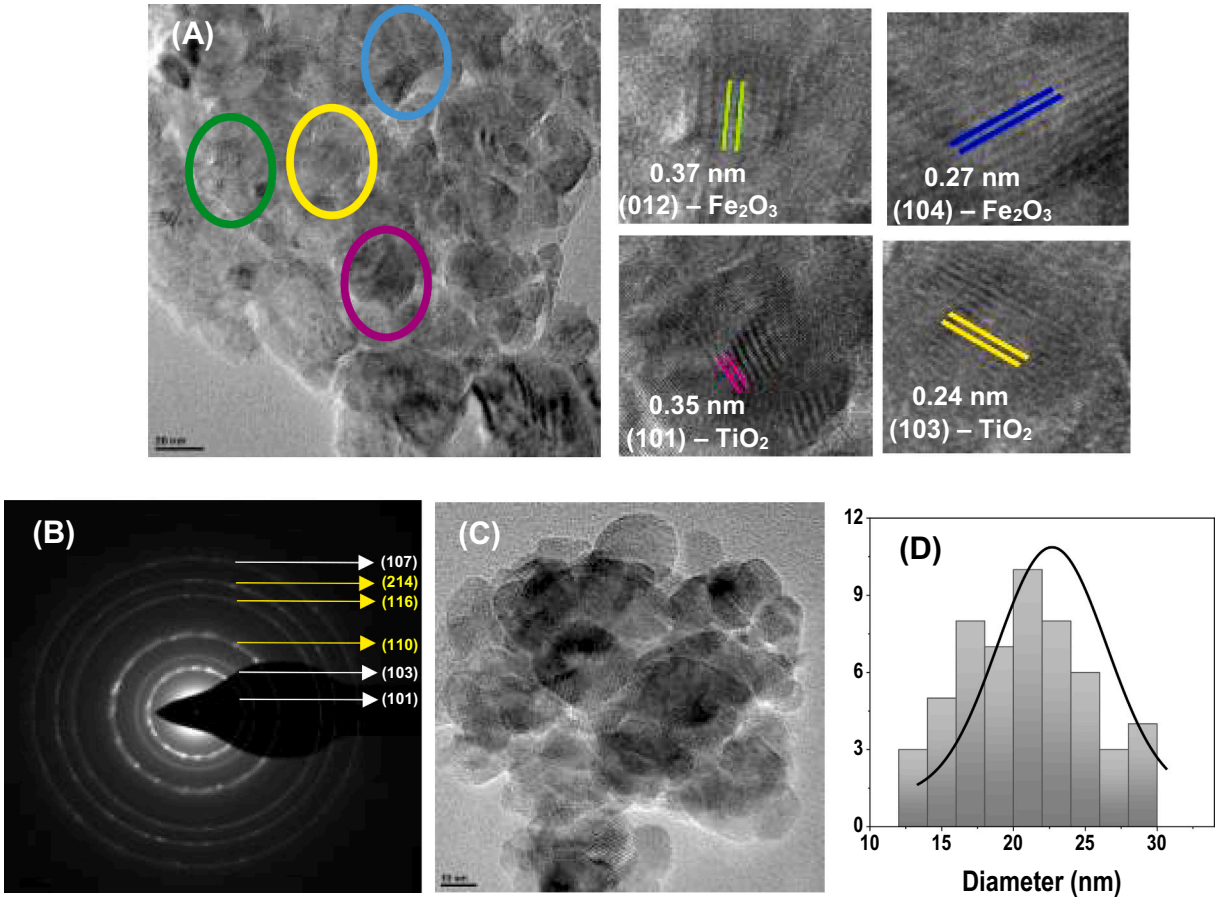

Fig. 7. $Fe_2O_3/Ti_2O/Al\text{-}PILC_{BE}$ (10 wt% Ti and 20 wt% Fe): (A) TEM and lattice fringes for TiO_2 (white) and Fe_2O_3 (yellow). (B) SAED pattern of the catalyst. (C and D) TEM and particle size distribution curve. (For interpretation of the references to colour in this figure legend, the reader is referred to the web version of this article.)

$$ln\frac{C_p}{C_{p0}} = -k_1 t \tag{6}$$

The pseudo-first-order rate constant is obtained from the slope calculated using the linear least-squares fit for the logarithmic plot of the data.

The pseudo-second-order model was also studied, using the following equations:

$$-\frac{dC_p}{dt} = k_2 C_P^2 \tag{7}$$

$$\frac{t}{C_t} = \frac{1}{k_2\, C_e^{\,2}} + \frac{t}{C_e} \tag{8}$$

where k_2 is the pseudo-second-order rate constant, and C_t and C_e the concentration of the pollutant (μmol/dm^3) at time t and equilibrium, respectively.

To choose the model that best fits the experimental data, a comparison of both the adjusted R-squared (R^2) and the residual sum of squares (RSS) was taken into account [41]. The RSS compares the experimental and calculated value according to the kinetic model. Smaller RSS values indicate a similarity between the experimental and calculated data, while higher values suggest that the model poorly explains the experimental data.

To evaluate the experimental results obtained in this work, we used a hypothesis test at 5 % significance level, the F test for comparison of variances, and analysis of conglomerates using Statgraphics (Centurion) and OriginPro (version 9).

2.5. By-product identification

The by-products obtained in the Fenton and photo-Fenton catalytic degradation of all three pollutants were identified by mass spectrometry. An UHPLC (Ultimate 3000 - Dionex) coupled to an UV detector and an electrospray ionization (ESI) mass spectrometer (amaZon SL - Bruker Daltonics) operating in negative mode and a C18 column (HALO, 2.1 × 150 mm, 4.6 μm particle size) were used for this purpose. A mixture of ACN:water (0.25 % formic acid) with a volume ratio of 60:40 was used as the mobile phase, at a flow rate of 0.5 cm^3/min. Each sample (10 μL) was analyzed in full-scan mode (range of 50 to 600 m/Z) at a scan speed of 0.20 scans/s.

The experiments to identify the by-products in both Fenton and photo-Fenton reactions were carried out by replicating the experiments with the catalyst that took longer for the conversions, to ensure identification of the maximum possible number of by-products during the experiment. The aliquots analyzed during the reaction were sampled at the same sampling times as in the previous experiments. All samples were diluted (1:10) before analysis in the HPLC-MS system. Finally, the by-products formed by all three target organic pollutants were tentatively identified by comparing the molecular ion and respective mass fragmentation pattern with those found in the literature with the aid of the NIST Mass Spectral Library.

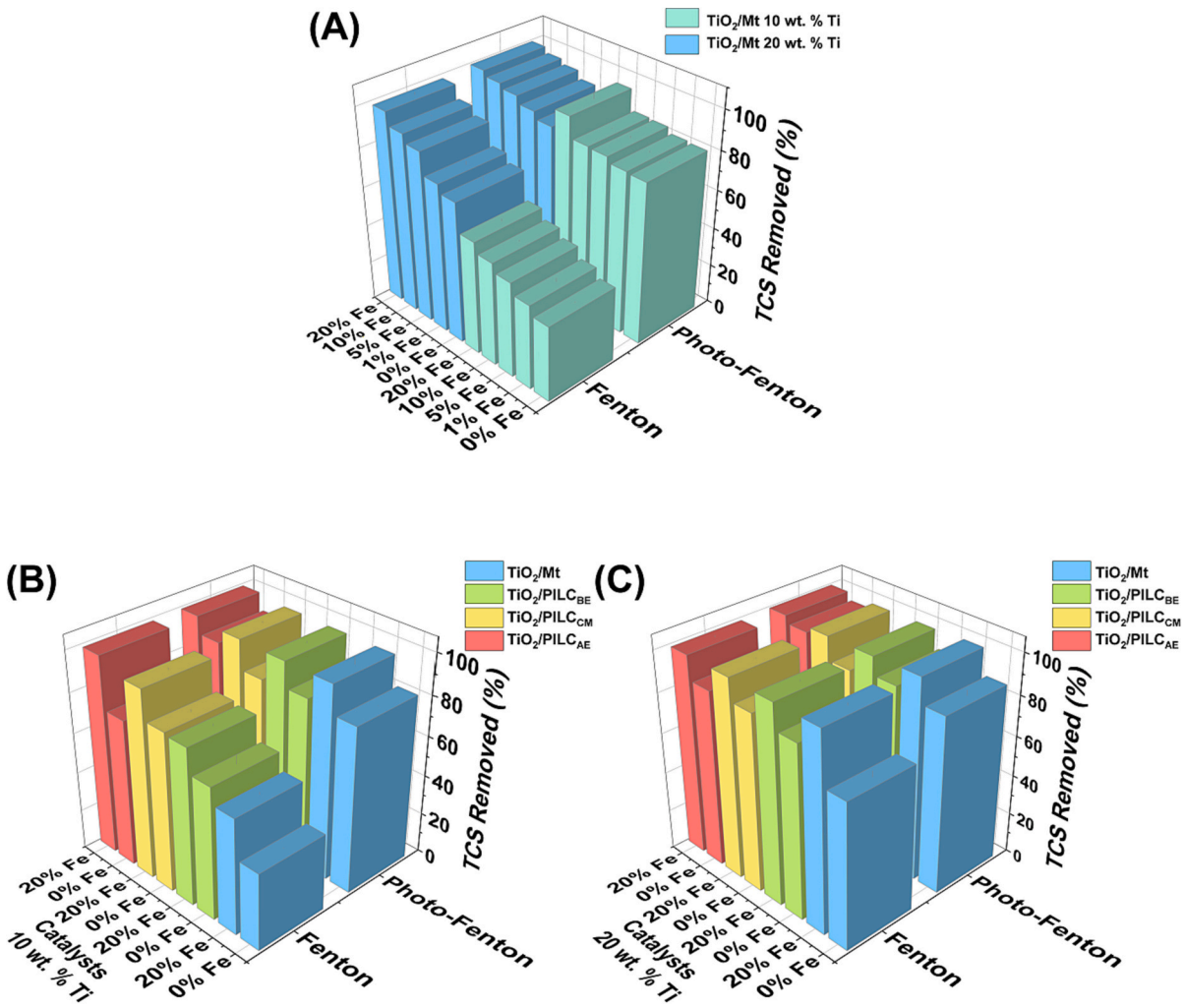

Fig. 8. Removal percentages (%) for TCS at 90 μmol/dm^3 as initial pollutant concentration, using: (A) TiO_2/Mt (10 and 20 wt% Ti) and Fe_2O_3/TiO_2/Mt (10 and 20 wt% Ti) with different amounts of iron (1–20 wt%), (B and C) TiO_2/Al-PILC (10 and 20 wt% Ti) and Fe_2O_3/TiO_2/Al-PILC (10 and 20 wt% Ti, both at 20 wt% iron).

3. Results and discussion

3.1. Characterization of the catalysts

Analysis of all the catalysts synthesized was repeated once, using XRD and N_2 adsorption techniques, in order to gain a better understanding of their homogeneity and to study them by statistical analysis. The XRD patterns of the Mt and Al-PILC used as supports are presented in Fig. S1. The XRD results of the catalysts synthesized confirmed the presence of both TiO_2 (anatase phase) and Fe_2O_3 in the solids as a result of the identification of their characteristic peaks, as shown in Fig. 1. The Debye-Scherer equation (Eq. (9)) [42] was used to calculate the crystallite size of both TiO_2 and Fe_2O_3 particles in all samples (Fe_2O_3/TiO_2/Mt and Fe_2O_3/TiO_2/Al-PILC) from the XRD patterns. This was performed using the most intense diffraction peak (101) of the anatase phase, found at 25.31°, and the average of the two most intense peaks (104) and (110) for Fe_2O_3, found at 33.33° and 35.79°.

$$D = \frac{K\lambda}{\beta\, Cos\theta} \tag{9}$$

where D is crystal size (nm), K is the crystallite shape factor (0.89), and λ the X-ray wavelength. β is the width at half maximum (FWHM) of the respective peak and θ is the Bragg angle.

The XRD patterns of the catalysts are summarized in Figs. 1 and 2. Fig. 1 shows the XRD pattern for Mt, TiO_2/Mt (10 and 20 wt% Ti), and Fe_2O_3/TiO_2/Mt (10 and 20 wt% Ti with 20 wt% Fe, in both cases). Fig. 2 presents the XRD pattern of the three TiO_2/Al-PILC (10 and 20 wt% Ti), and Fe_2O_3/TiO_2/Al-PILC (10 and 20 wt% Ti with 20 wt% Fe, in both cases). The estimated value of the crystallite size for TiO_2-anatase in all samples, including Mt and Al-PILC, ranged from 18.52 ± 1.75 to 25.81 ± 0.22 nm, which is in agreement with the values reported previously [35,36,43]. All Mt samples at both titanium contents (10 and 20 wt%) impregnated with various iron loadings showed an increase in the Fe_2O_3 crystal size as the amount of iron used in the impregnation step increased, ranging from 16.05 ± 0.72 (Mt 10 wt% Ti and 1 wt% Fe) to 39.92 ± 7.70 nm (Mt 20 wt% Ti and 20 wt% Fe). The ANOVA of the crystal size values showed that there is only a statistically significant difference between the catalysts at 20 % Ti impregnated with various iron loadings ($p < 0.05$; 95 % confidence). The results revealed that the titanium content has a statistically significant effect on the crystal size ($p < 0.05$).

In the case of Al-PILC at both 10 and 20 wt% titanium, impregnated with 20 % iron, the crystal sizes ranged from 24.24 ± 0.40 (Al-PILC$_{BE}$ 10 wt% Ti and 20 wt% Fe) to 42.88 ± 1.99 nm (Al-PILC$_{CM}$ 20 wt% Ti and 20 wt% Fe. The statistical analysis of the data revealed that there is no statistically significant difference between the crystal sizes of the three Al-PILC ($p > 0.05$; 95 % confidence). The crystal sizes calculated in this work are in agreement with the values reported by other authors [43–45].

The textural characteristics of the supports are shown in Fig. S1 and

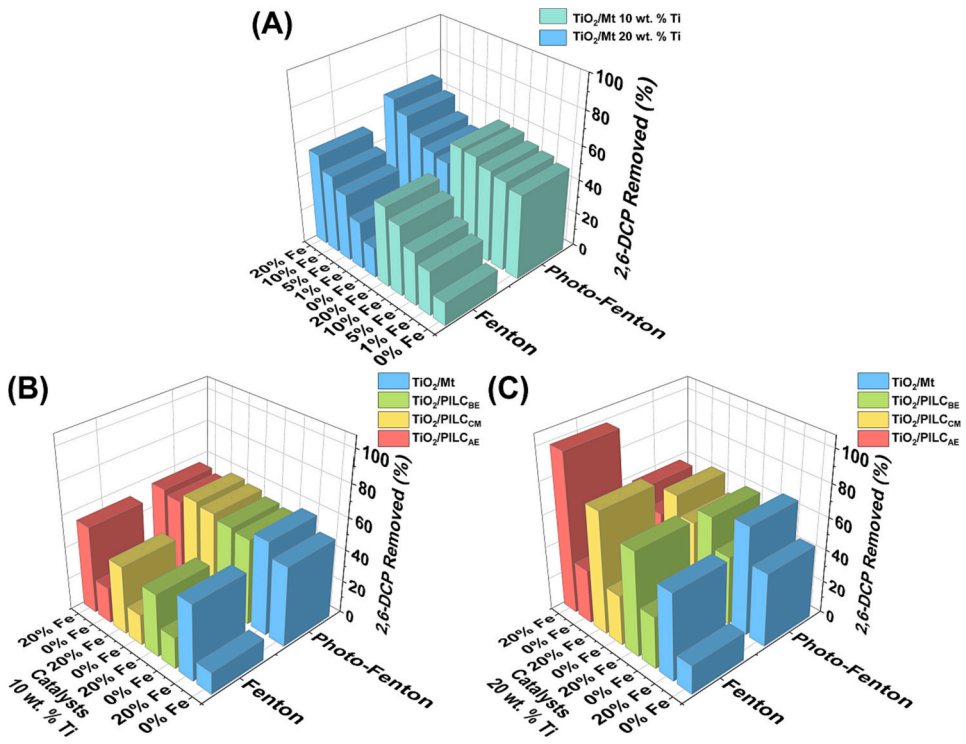

Fig. 9. Removal percentages (%) for 2,6-DCP at 90 μmol/dm^3 as initial pollutant concentration, using: (A) TiO_2/Mt (10 and 20 wt% Ti) and Fe_2O_3/TiO_2/Mt (10 and 20 wt% Ti) with different amounts of iron (1–20 wt%), (B and C) TiO_2/Al-PILC (10 and 20 wt% Ti) and Fe_2O_3/TiO_2/Al-PILC (10 and 20 wt% Ti, both at 20 wt% iron).

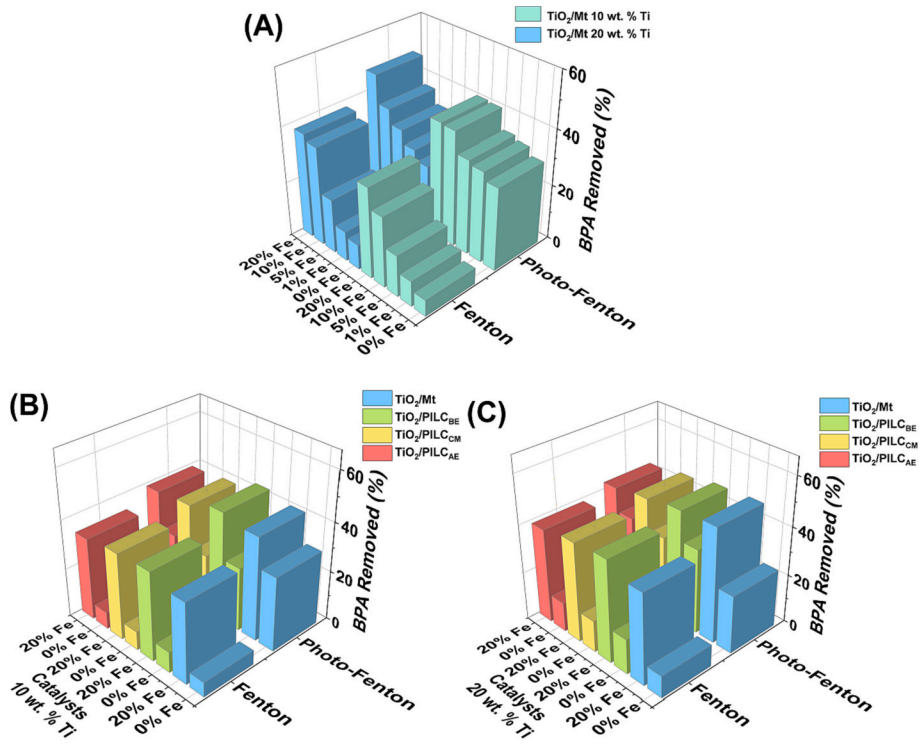

Fig. 10. Removal percentages (%) for BPA at 90 μmol/dm^3 as initial pollutant concentration, using: (A) TiO_2/Mt (10 and 20 wt% Ti) and Fe_2O_3/TiO_2/Mt (10 and 20 wt% Ti) with different amounts of iron (1–20 wt%), (B and C) TiO_2/Al-PILC (10 and 20 wt% Ti) and Fe_2O_3/TiO_2/Al-PILC (10 and 20 wt% Ti, both at 20 wt% iron).

the textural characteristics of the catalysts are summarized in Table 1 and Figs. 3 and 4. Table 1 lists the calculated specific surface areas (S_{BET}), average pore diameters (d_p), and total pore volumes (V_{Total}), and Fig. 3 shows the N_2 adsorption-desorption isotherms for TiO_2/Mt at 10 and 20 wt% Ti, and Fe_2O_3/TiO_2/Mt at 10 and 20 wt% Ti, with various iron contents (1–20 wt%). Fig. 4 shows the N_2 adsorption-desorption isotherms for the different Fe_2O_3/TiO_2/Mt and Fe_2O_3/TiO_2/Al-PILC synthesized at both titanium concentrations (10 and 20 wt% Ti), with

Table 2
Percentages removed of all three pollutants by both Fenton and photo-Fenton reactions in both single and mixture component experiments.

Total pollutant removed (%)						
Catalysts at 20 % Ti, 20 % Fe	TCS		2,6 DCP		BPA	
	Single-component	Mixture-component	Single-component	Mixture-component	Single-component	Mixture-component
	Mean ± SD	Mean ± SD	Mean ± SD	Mean ± SD	Mean ± SD	Mean ± SD
Fenton reaction						
None	32.83 ± 1.23	23.24 ± 0.81	12.91 ± 0.43	6.54 ± 0.98	8.61 ± 0.60	7.30 ± 1.01
Mt	98.30 ± 1.16	98.37 ± 0.80	53.71 ± 2.97	47.34 ± 1.90	37.77 ± 1.04	35.34 ± 0.45
$PILC_{BE}$	98.44 ± 0.86	99.44 ± 0.55	64.42 ± 1.37	36.31 ± 2.25	42.24 ± 0.55	41.95 ± 0.26
$PILC_{CM}$	98.94 ± 0.28	96.49 ± 2.00	75.49 ± 1.31	56.98 ± 1.79	41.14 ± 0.53	40.88 ± 0.37
$PILC_{AE}$	99.21 ± 0.90	93.60 ± 0.02	98.78 ± 0.47	94.68 ± 1.96	38.98 ± 0.66	38.68 ± 0.66
Photo-Fenton reaction						
None	33.36 ± 1.24	16.22 ± 1.31	13.23 ± 0.64	7.19 ± 0.71	8.65 ± 0.33	6.97 ± 0.97
Mt	99.74 ± 0.36	58.30 ± 1.56	67.26 ± 1.06	61.71 ± 1.16	47.65 ± 1.27	47.50 ± 0.57
$PILC_{BE}$	99.09 ± 0.29	67.40 ± 0.44	61.21 ± 0.73	57.45 ± 2.10	47.04 ± 0.61	44.92 ± 1.52
$PILC_{CM}$	99.00 ± 0.17	61.67 ± 0.49	63.21 ± 0.81	61.16 ± 1.49	45.02 ± 1.13	44.67 ± 0.78
$PILC_{AE}$	99.95 ± 0.08	61.14 ± 0.36	57.75 ± 0.41	54.40 ± 3.19	43.15 ± 1.11	42.58 ± 2.09

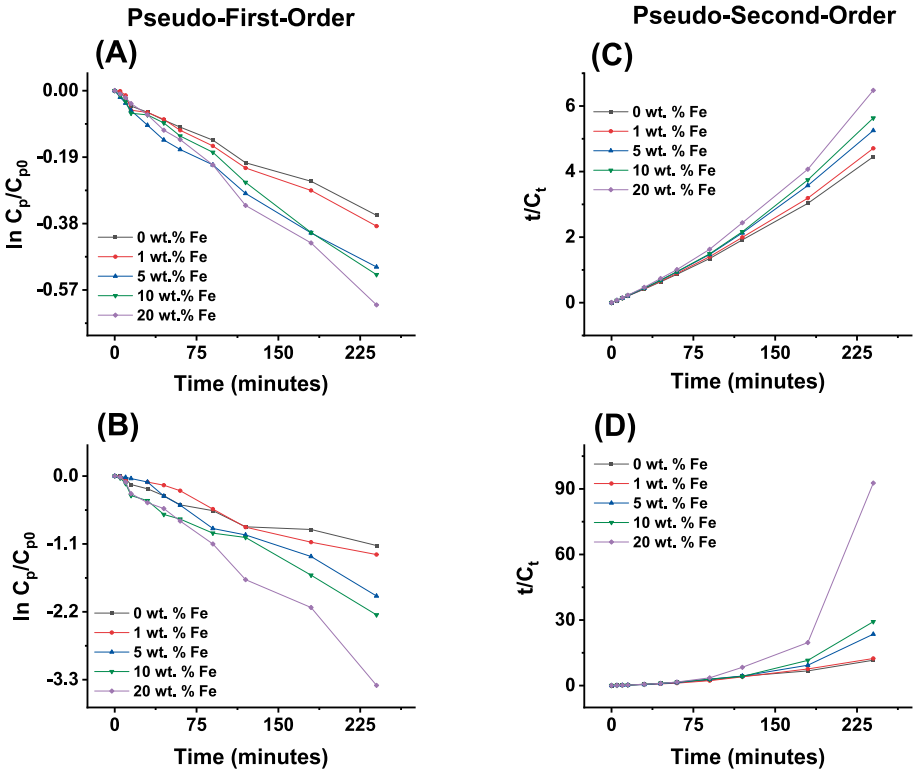

Fig. 11. Plots of pseudo-first- (A and B) and pseudo-second-order kinetic models (C and D) for the degradation of TCS, using Fe_2O_3/TiO_2/Mt at 10 wt% Ti (A and C) or 20 wt% Ti (B and D), both at different iron loadings (1–20 wt%).

20 wt% Fe. The adsorption isotherms obtained, which are considered to be Type II (according to the IUPAC classification) [46], are characteristic of PILC. The hysteresis loops of the isotherms exhibit a broad pore-size distribution [36]. In the case of the catalysts synthesized using Mt as the catalytic support, statistical analysis of the S_{BET} data showed that there is only a significant difference for those at 20 wt% Ti with various iron contents (1–20 % Fe; $p < 0.05$; 95 % confidence). The multifactorial analysis of the S_{BET} data for all catalysts in Table 1 showed that both factors (titanium and iron content) have a statistically significant effect ($p < 0.05$; 95 % confidence) only for those catalysts synthesized using Al-PILC as catalytic support. For Fe_2O_3/TiO_2/Mt, only the titanium content has a significant effect on S_{BET} value (95 % confidence). These results highlight both the relationship between the crystallite size and the S_{BET} area of the catalysts, and the relevance of the iron/titanium ratio used in their synthesis.

The morphology of all the catalysts studied in this work was evaluated by SEM and TEM. The micrographs are presented in Fig. 5 (SEM) and Fig. 6 (TEM). These micrographs (Figs. 5.A and 6.A) show the surface morphology of all the catalytic supports used, clearly highlighting the differences between the mineral clay and the pillared clays used. Mt has a fluffy and smooth appearance with irregular flakes, while Al-PILC shows a uniform morphology. The SEM and TEM images in Figs. 5 and 6 show the different catalysts at 20 wt% Ti with 0 wt% Fe (B), and 20 wt% Ti with 20 wt% Fe (C). A comparison of those micrographs also reveals the significant change in the structure of the supports upon incorporation of TiO_2 and Fe_2O_3 into the structure. Figs. 5.C and 6.C (20 wt% Ti and 20 wt% Fe) show disordered and exfoliated structures. The morphological features observed in the SEM and TEM images suggest

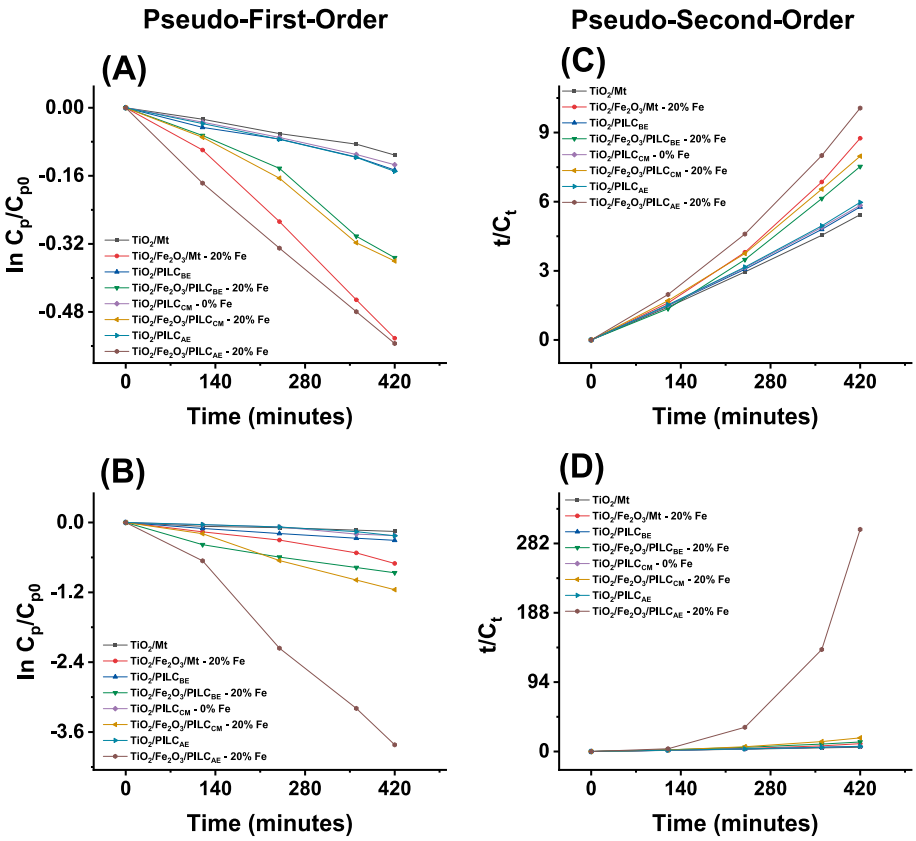

Fig. 12. Plots of pseudo-first- (A and B) and pseudo-second-order kinetic models (C and D) for the degradation of TCS using the different catalysts at 10 wt% Ti (A and C) or 20 wt% Ti (B and D), both with different iron loadings (1–20 wt%).

formation of the particles on the external surface of the catalytic supports, in agreement with other authors [36]. The micrographs of the Fe_2O_3/TiO_2/Mt and Fe_2O_3/TiO_2/Al-PILC catalysts synthesized under the conditions of this study demonstrate the formation of nanostructures with an average particle size of <50 nm, which is in agreement with the XRD results and with other authors who have synthesized TiO_2/Fe_2O_3 nanoparticles [47].

Fig. 7 (A) shows a TEM micrograph for Al-$PILC_{BE}$ at 10 wt% Ti and 20 wt% Fe. The lattice fringes of TiO_2 (pink and yellow) and Fe_2O_3 (green and blue) correspond to the (101), (103), (012), and (104) planes, with a fringe distance of 0.35, 0.24, 0.37, and 0.27 nm, respectively. Fig. 7 (B) presents the selected area electron diffraction (SAED) pattern for the Fe_2O_3/TiO_2/Al-$PILC_{BE}$ catalyst, which corroborates the XRD findings regarding the presence of TiO_2 and Fe_2O_3 in the catalysts synthesized. The crystallographic planes (101), (103), and (107) correspond to TiO_2, while the crystallographic planes (110) and (116) and (214) correspond to Fe_2O_3. For all catalysts, the size of the particles calculated from the TEM images is in agreement with the XRD results. Fig. 7 (D) shows the particle size distribution curve calculated for Al-$PILC_{BE}$ with 10 wt% Ti and 20 wt% Fe and also the uniform distribution of the particles, with an average diameter of 21 nm.

Finally, as mentioned in the experimental procedure, EDX was used to monitor the average elemental composition of the nanocomposites synthesized and confirm the purity of the catalysts. Fig. S2 shows the elemental mapping analysis of the catalysts at 20 % Ti and 20 % Fe. The EDX results confirmed the presence of both TiO_2 and Fe_2O_3 in all catalysts synthesized and, as can be seen in Table S1, they did not contain impurities. These values also show that both contents (TiO_2 and Fe_2O_3) were successfully controlled during the synthesis given the similarity between the experimental content and the theoretical value used during impregnation. The relative error of the impregnations ranged from 0.4 % to 12.0 % and was lower for impregnation with titanium (0.4–7.8 %) than for impregnation with iron (7.1–12.0 %). The highest relative error for the titanium and iron impregnations was found for the synthesis of Fe_2O_3/TiO_2/Al-$PILC_{BE}$.

3.2. Fenton and photo-Fenton-like reactions

In the single-component experiments, the experimental times (Fenton and photo-Fenton) were selected on the basis of the time required to remove the maximum quantity of the respective pollutant from the solution in all cases. In the Fenton experiments for TCS, 2,6-DCP, and BPA, these times were 240, 420, and 540 min, respectively. The times required for the photo-Fenton experiments were 30 min for TCS and 90–120 min for 2,6-DCP and BPA. The duration of the equimolar-mixture experiments was established on the basis of the time required to remove the slowest degraded pollutant in the single-component experiments.

The percentage of TCS, 2,6-DCP, and BPA removed by the catalysts in the single-component experiments, after 240 (TCS), 420 (2,6-DCP), and 540 (BPA) minutes of Fenton-like reaction and after 30 min of photo-Fenton-like reaction, are summarized in Figs. 8, 9 and 10, respectively. As can be seen in Figs. 8 and 9, almost complete removal (~100 %) of TCS and 2,6-DCP was achieved. In the case of TCS, this was possible in both the Fenton and photo-Fenton processes, irrespective of the four catalytic supports evaluated. For 2,6-DCP and BPA, however, better results were obtained when using Al-$PILC_{AE}$ and Al-$PILC_{BE}$ as the catalytic supports. The three were at the highest loading of both titanium and iron. The maximum BPA removed in the Fenton-like reaction was 42.24 %. As the figures reveal, a reaction time of 30 min was insufficient to achieve the complete removal of 2,6-DCP and BPA in the photo-Fenton-like reaction. Finally, for all three pollutants, the percentage removed was lower in the equimolar mixture-component solutions than in the single-component experiments, with values up to 1.77-,

Table 3
Rate parameters for the conversion of TCS, 2,6-DCP and BPA by Fenton (without UV radiation) and photo-Fenton (with UV radiation) reactions, using the catalysts with highest conversion values.

Solid	Radiation	Pseudo first order model			Pseudo second order model		
	UV	k_1	RSS	R^2	k_2	RSS	R^2
TCS							
None	Without	0.003	0.002	0.987	0.017	0.128	0.993
	With	0.004	0.004	0.978	0.017	0.072	0.983
TiO_2/Fe_2O_3/Mt – 10 wt% Ti and 20 wt% Fe	Without	0.003	0.001	0.997	0.026	0.980	0.977
	With	0.167	1.811	0.890	1.541	236.837	0.842
TiO_2/Fe_2O_3/Mt – 20 wt% Ti and 20 wt% Fe	Without	0.013	0.143	0.987	0.291	2327.992	0.693
	With	0.180	0.983	0.946	2.361	666.925	0.816
TiO_2/Fe_2O_3/Al-PILC$_{BE}$ – 20 wt% Ti and 20 wt% Fe	Without	0.030	0.231	0.982	0.886	4755.209	0.901
	With	0.275	0.084	0.991	1.049	51.185	0.729
TiO_2/Fe_2O_3/Al-PILC$_{CM}$ – 20 wt% Ti and 20 wt% Fe	Without	0.032	0.599	0.960	0.864	8640.696	0.842
	With	0.272	0.337	0.965	1.126	61.805	0.916
TiO_2/Fe_2O_3/Al-PILC$_{AE}$ – 20 wt% Ti and 20 wt% Fe	Without	0.035	0.166	0.978	0.614	557.321	0.975
	With	0.496	0.143	0.988	3.677	202.234	0.770
2,6-DCP							
None	Without	0.001	0.000	0.980	0.013	0.003	0.999
	With	0.001	0.000	0.989	0.013	0.003	0.999
TiO_2/Fe_2O_3/Mt – 10 wt% Ti and 20 wt% Fe	Without	0.001	0.003	0.990	0.015	0.835	0.979
	With	0.026	0.014	0.961	0.028	0.013	0.968
TiO_2/Fe_2O_3/Mt – 20 wt% Ti and 20 wt% Fe	Without	0.002	0.014	0.962	0.024	3.516	0.962
	With	0.037	0.003	0.996	0.037	0.039	0.948
TiO_2/Fe_2O_3/Al-PILC$_{BE}$ – 20 wt% Ti and 20 wt% Fe	Without	0.002	0.021	0.977	0.030	3.007	0.984
	With	0.017	0.008	0.947	0.020	0.006	0.973
TiO_2/Fe_2O_3/Al-PILC$_{CM}$ – 20 wt% Ti and 20 wt% Fe	Without	0.003	0.015	0.986	0.043	15.977	0.934
	With	0.028	0.001	0.999	0.031	0.020	0.963
TiO_2/Fe_2O_3/Al-PILC$_{AE}$ – 20 wt% Ti and 20 wt% Fe	Without	0.009	0.371	0.972	0.608	1731.999	0.763
	With	0.024	0.008	0.975	0.026	0.008	0.980
BPA							
None	Without	0.001	0.000	0.969	0.012	0.001	1.000
	With	0.001	0.000	0.986	0.013	0.001	1.000
TiO_2/Fe_2O_3/Mt – 10 wt% Ti and 20 wt% Fe	Without	0.001	0.001	0.988	0.016	0.547	0.991
	With	0.019	0.007	0.965	0.020	0.004	0.983
TiO_2/Fe_2O_3/Mt – 20 wt% Ti and 20 wt% Fe	Without	0.001	0.002	0.984	0.018	0.868	0.987
	With	0.021	0.001	0.996	0.022	0.008	0.971
TiO_2/Fe_2O_3/Al-PILC$_{BE}$ – 20 wt% Ti and 20 wt% Fe	Without	0.001	0.001	0.990	0.019	1.072	0.986
	With	0.016	0.003	0.978	0.022	0.003	0.989
TiO_2/Fe_2O_3/Al-PILC$_{CM}$ – 20 wt% Ti and 20 wt% Fe	Without	0.001	0.000	0.998	0.019	0.743	0.991
	With	0.015	0.003	0.972	0.021	0.002	0.991
TiO_2/Fe_2O_3/Al-PILC$_{AE}$ – 20 wt% Ti and 20 wt% Fe	Without	0.001	0.001	0.985	0.014	0.506	0.989
	With	0.014	0.000	0.996	0.020	0.003	0.986

16.82-, and 1.33-times smaller for TCS, 2,6-DCP, and BPA, respectively.

The percentages of the three pollutants removed under both Fenton- and photo-Fenton-like conditions were higher, in both single- and mixed-component systems, for the catalysts containing 20 wt% titanium than for those containing 10 wt% titanium. Additionally, in both Fenton and photo-Fenton experiments, the percentages of the three pollutants removed increased as the iron content (wt%) increased (see Figs. 8–10). Table S2 shows the percentages of all three pollutants removed in both single- and mixed-component solutions under both Fenton and photo-Fenton conditions, using the catalysts synthesized with 10 wt% Ti and 20 wt% Ti and the highest iron load (20 wt%) in both cases. The reaction times required to achieve these values were 240 (TCS), 420 (2,6-DCP) and 540 min (BPA) for the Fenton reaction, and 30 min for all three pollutants in the photo-Fenton reaction. Table 2 shows the percentages obtained at the highest iron concentration which are those that gave the highest conversion. For the complete removal of 2,6-DCP in the photo-Fenton process, a reaction time of at least 90 min was required for the three Al-PILCs and 120 min for the Mt, while a time of at least 120 min was needed to reach the highest removal of BPA (70.25–80.14 %) in the photo-Fenton process. The time required to remove the pollutants in the photo-Fenton-like reaction was less than that required for the Fenton-like reaction. A comparison of the amounts removed at the same sampling times revealed higher values for the photo-Fenton reaction than for the Fenton reaction at every sampling time, with the highest values being achieved when the catalysts used contained 20 wt% Ti and 20 wt % Fe. This higher degradation rate for the photo-Fenton-like process indicates the successful narrowing of the bandgap. This is possible due to both the well-formed anatase phase, as confirmed by XRD, and the presence of Fe^{3+} in the TiO_2 conduction layer, which allows the excited electrons to react with the Fe^{3+} ions, thereby preventing or reducing electron-hole recombination [13,48]. The improvement in the catalytic performance of the catalysts as the iron load increased could also be due to the introduction of oxygen vacancies by the iron, which results in the formation of surface hydroxyl groups, as explained by other authors [13]. These results clearly show the positive synergistic effect of the UV/$TiO_2/Fe_2O_3/H_2O_2$ system in the oxidative degradation of the pollutants studied herein. This synergistic acceleration in the oxidative degradation process agrees with results reported by other authors [49].

Statistical analysis of all data for every pollutant was carried out by performing a multi-factor analysis of variance involving five factors: iron and titanium content in the catalyst used; catalytic support; system (single compound or mixture of the three pollutants); and UV (presence or absence). The results revealed that all five factors have a statistically significant effect on the total removal of 2,6-DCP ($p < 0.05$), but only four of them (iron and titanium content, catalytic support, and system) on the total removal of TCS, and three (iron and titanium content, and UV) on the total removal of BPA ($p < 0.05$, with 95 % confidence). In all three cases, the factor which contributed most to the variance of the

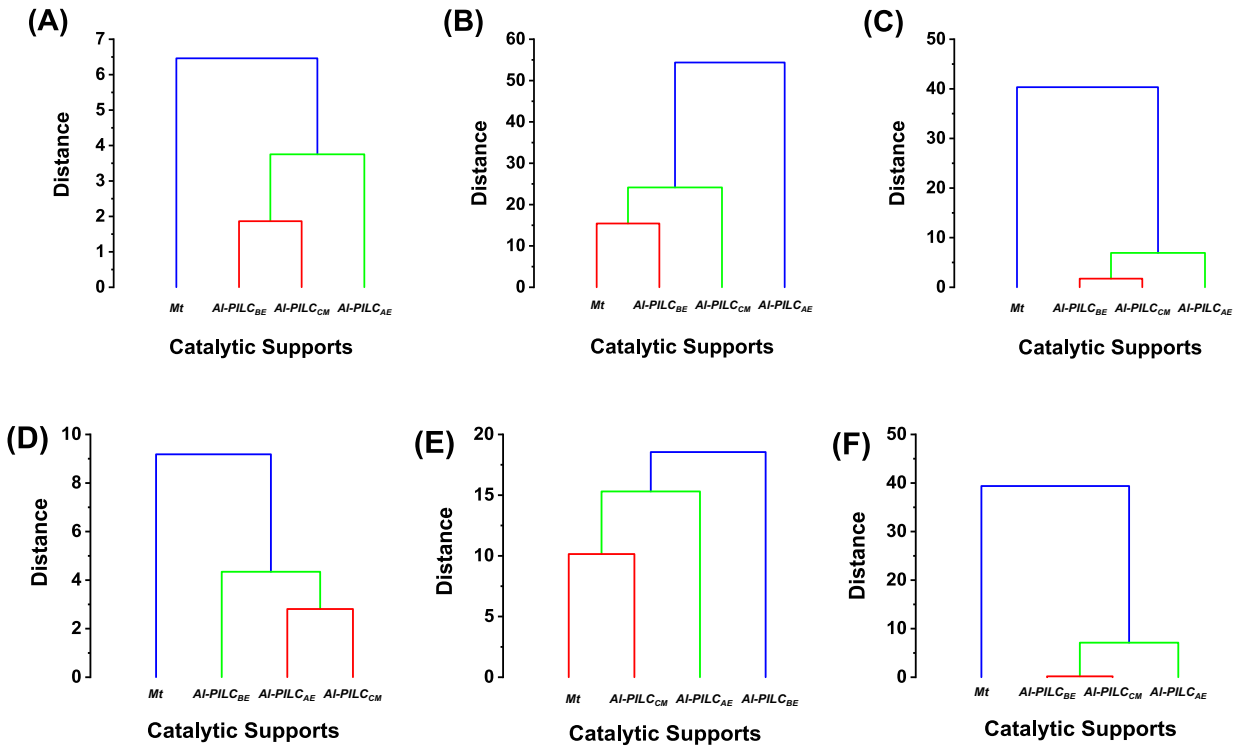

Fig. 13. Dendrogram showing the relationship between the amount of BPA (A and D), 2,6-DCP (B and E), and TCS (C and F) adsorbed (%), converted (%) and total removed (%) by the catalytic supports at the highest titanium and iron content (20 wt%) under both Fenton-like (A–C) and photo-Fenton-like (D–F) conditions.

total removal was UV, which contributes 94.35 % (2,6-DCP), 50.45 % (TCS), and 73.02 % (BPA), followed by the iron content in the case of 2,6-DCP (5.29 %) and BPA (26.63 %), and system in the case of TCS (43.59 %). These findings corroborate the improvement in the degradation efficiency due to the use of UV radiation. A statistical analysis was also carried out focusing on the catalytic supports. For Mt, the UV factor contributed most to the variance in the total removal of all three pollutants (84.18 % for 2,6-DCP, 45.34 % for TCS, and 99.71 % for BPA). In the case of the three Al-PILC, the data showed that the total removal behavior differs between the three pollutants studied. Thus, for the removal of BPA, three factors, namely iron and titanium content and UV, have a significant effect, with iron content, accounting for 62.82 % (Al-PILC$_{BE}$), 68.57 % (Al-PILC$_{CM}$), and 62.16 % (Al-PILC$_{AE}$), contributing most to this variance. For the removal of 2,6-DCP, two factors, namely system and UV, have a statistically significant effect, and the factor which contributed most to the variance was UV, accounting for 99.61 % (Al-PILC$_{BE}$), 93.73 % (Al-PILC$_{CM}$), and 78.82 % (Al-PILC$_{AE}$). Finally, for TCS removal, three factors, namely titanium content, system, and UV (Al-PILC$_{BE}$, Al-PILC$_{CM}$), and iron content, system, and UV (Al-PILC$_{AE}$), have a significant effect. In this case, the factor which contributed most to the variance for Al-PILC$_{BE}$ and Al-PILC$_{AE}$ was UV, accounting for 76.82 % (Al-PILC$_{BE}$) and 53.91 % (Al-PILC$_{CM}$), followed by system (22.14 % for Al-PILC$_{BE}$ and 45.94 % for Al-PILC$_{AE}$), while for Al-PILC$_{CM}$ the factor which contributed most to the variance in the total removal of TCS was system (56.24 %), followed by UV (43.53 %). The conversion data for all three pollutants were analyzed statistically by way of a multifactor analysis. For TCS and 2,6-DCP, two factors, namely titanium content and UV (presence or absence), have a statistically significant effect on the conversion of TCS ($p < 0.05$, with 95 % confidence). For BPA, three factors, namely iron and titanium content and UV (presence or absence) have a statistically significant effect on the conversion. For all three pollutants, UV was the factor that contributed most to the variance in pollutant conversion, accounting for 98.83 % (TCS), 89.45 % (2,6-DCP), and 77.86 % (BPA).

A comparison of both pseudo-first- and pseudo-second-order kinetic plots for TCS in the Fenton process can be found in Figs. 11 and 12. Fig. 11 shows the plots for Fe_2O_3/TiO_2/Mt at both 10 and 20 wt% Ti with the iron loadings tested in this work (1–20 wt%), and Fig. 12 the catalysts at 10 and 20 wt% Ti with 20 wt% Fe. The kinetic parameters for all three pollutants can be found in Table 3 for both the Fenton (without UV radiation) and photo-Fenton (with UV radiation) reactions. This table gives the parameters obtained from the curve fitting for both models (pseudo-first- and pseudo-second-order reactions). Tables S3–S5 give the kinetic parameters for all catalysts used in this work. For the three pollutants studied, the higher regression values (0.890–0.997 for TCS, 0.935–0.999 for 2,6-DCP, and 0.946–0.998 for BPA) and the lower residual sum of squares (RSS) values (0.001–1.811 for TCS, 1.21×10^{-4}–0.371 for 2,6-DCP, and 2.59×10^{-5}–0.007 for BPA) obtained using the pseudo-first-order kinetic equation show that this kinetic best fits the experimental data for conversion of all the pollutants in both the Fenton and photo-Fenton processes. The half-life ($\tau_{1/2}$) values were calculated using Eq. (10), in which k_1 is the pseudo-first-order rate constant.

$$\tau_{1/2} = \frac{0.693}{K_1} \tag{10}$$

Table S6 gives the calculated half-life ($\tau_{1/2}$) values for the Fenton and photo-Fenton processes. The results confirmed that the photo-Fenton-like process is more efficient for degrading all three pollutants.

As was mentioned in the experimental section, the Fenton and photo-Fenton catalytic degradation experiments started after 15 min of adsorption in the dark in the presence of the corresponding catalyst. The adsorption results for the catalysts showed that the amount of the three pollutants adsorbed in both single- and mixed-component systems was higher for the catalysts impregnated with 20 % titanium than for those impregnated with 10 % Ti. Additionally, in both cases (10 and 20 % Ti), the amount adsorbed increased as the iron content (%) increased for all catalysts used. A statistical analysis of the adsorption data was conducted for each pollutant involving four factors, namely catalytic support used, iron and titanium content in the catalyst, and system (single

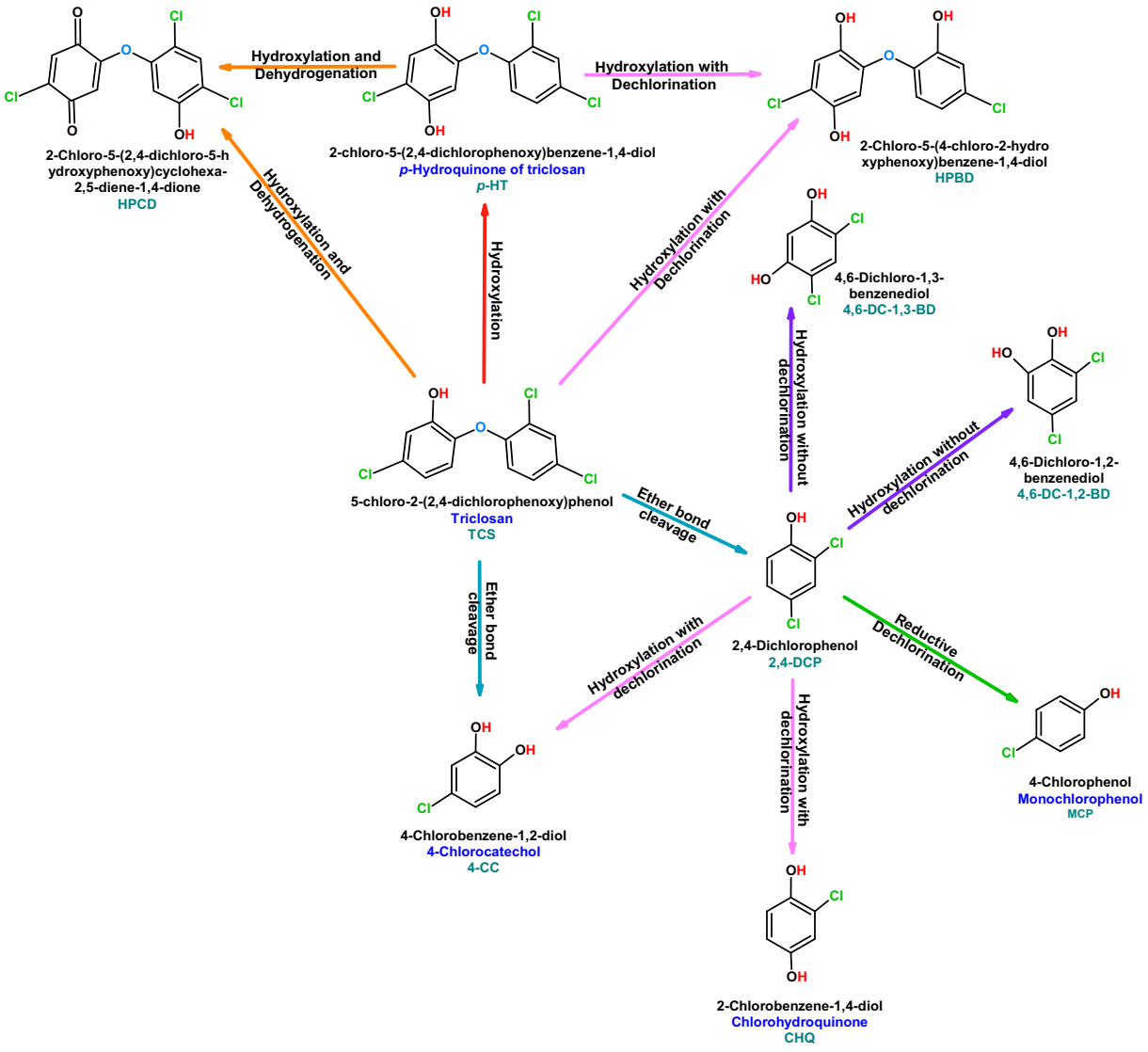

Fig. 14. Possible degradation pathway of TCS.

compound or mixture of the three pollutants). The results revealed that all four factors have a statistically significant effect on adsorption for all three pollutants ($p < 0.05$, with 95 % confidence). However, the factor that contributed most to the variance of the adsorption differed for the three pollutants. Thus, for 2,6-DCP, it was the system (single- or mixed-component), which contributed 55.29 % to the variance in adsorption, while for BPA this factor was the iron content (71.51 %), and for TCS the catalytic support used (33.64 %). A statistical analysis of the adsorption data for the catalytic supports used was conducted for each of the three pollutants including three factors, namely iron and titanium content and system (single compound or mixture of the three pollutants). The results showed that all three factors have a statistically significant effect on the adsorption of all three pollutants for Mt ($p < 0.05$), while these three factors have a statistically significant effect on the adsorption of 2,6-DCP and TC for all three Al-PILC. In the case of BPA adsorption on Al-PILC, two factors, namely iron and titanium content, have a significant effect. In the case of BPA and TCS, iron content was the factor that contributed most to the variance of adsorption on the three PILC and two PILC, respectively. Thus, the iron content contributed 85.84 % (Al-$PILC_{BE}$), 72.62 % (Al-$PILC_{CM}$), and 99.01 % (Al-$PILC_{AE}$) to the variance in BPA adsorption, and 32.23 % (Al-$PILC_{BE}$) and 40.99 % (Al-$PILC_{CM}$) to the variance in TCS adsorption. In the case of Al-$PILC_{AE}$, the factor that contributed most to the variance in TCS adsorption was system (single compound or mixture), accounting for 68.05 % of the variance. Finally, system also was the factor that contributed most to the variance of 2,6-DCP adsorption, accounting for 55.68 % (Al-$PILC_{BE}$), 83.48 % (Al-$PILC_{CM}$), and 69.87 % (Al-$PILC_{AE}$). These results reveal that adsorption of the pollutants plays an important role in the total removal of TCS, which was the most adsorbed pollutant (5.44–54.55 %), 2,6-DCP (0.29–15.4 %) and BPA (0.01–11.58 %). The successful use of TiO_2/clay hybrids as adsorbents for the removal of pollutants has been reported previously [36].

Finally, with the aim of clarifying the similarities and differences between the changes in adsorption, conversion, and total removal in both reactions (Fenton- and photo-Fenton-like) by the catalysts that showed the best results (20 wt% Ti and 20 wt% Fe), a hierarchical cluster analysis was carried out using the nearest neighbor method. The results are presented in Fig. 13 for BPA (A and D), 2,6-DCP (B and E), and TCS (C–F) in both Fenton-like (A–C) and photo-Fenton-like (D–F) reactions. The cluster in Fig. 13 (A), for example, shows how, for BPA, adsorption and conversion by the catalyst (20 wt% Ti and 20 wt% Fe) synthesized using Al-$PILC_{BE}$ as catalytic support are very similar to those obtained using Al-$PILC_{CM}$. It also reveals that, in this case, somewhat different values were obtained for the catalyst synthesized using Mt as catalytic support. The clusters in Fig. 13 show how the similarities and differences between the catalysts in the Fenton-like reaction (A) only

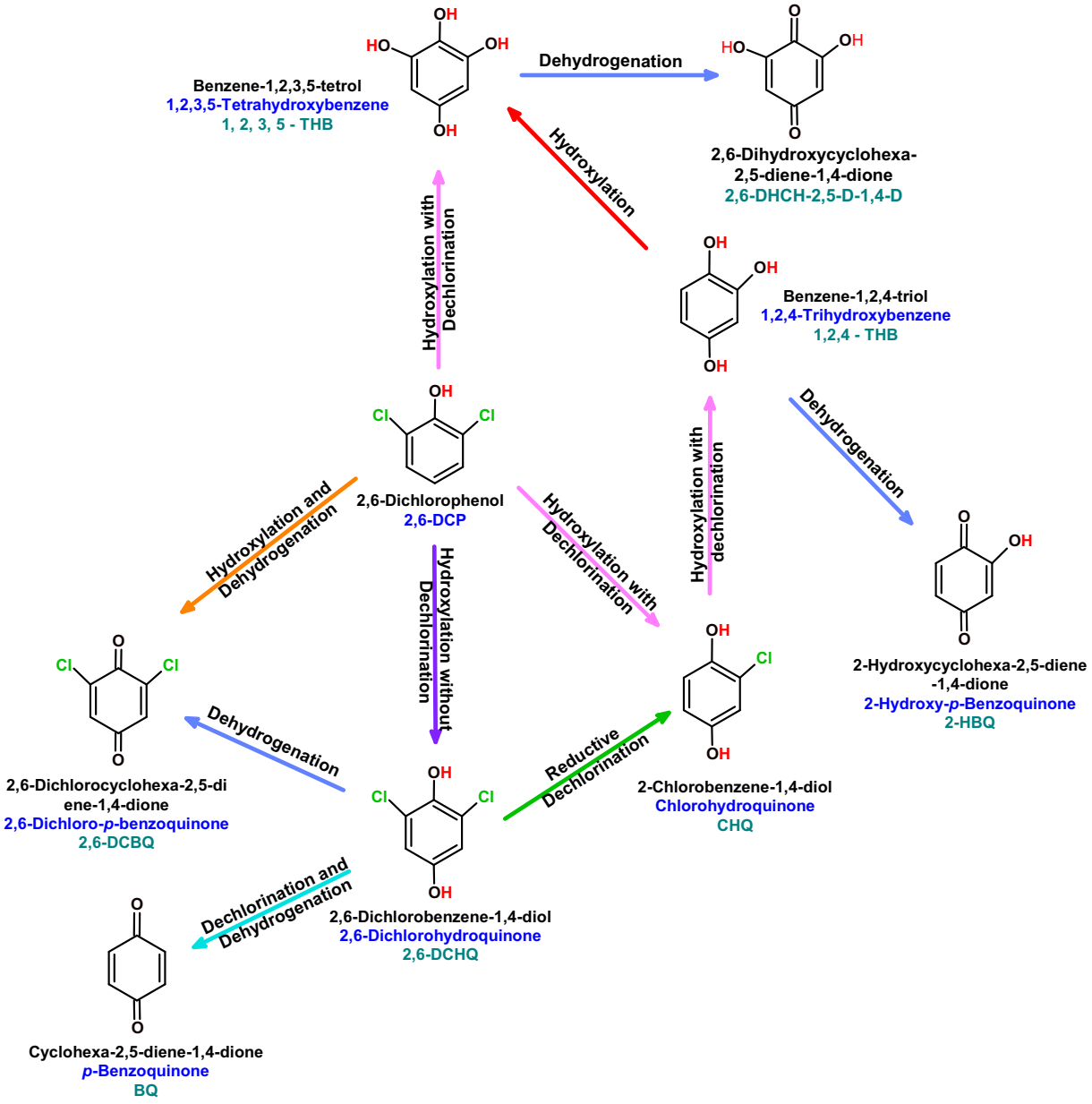

Fig. 15. Possible degradation pathway of 2,6-DCP.

differ from those observed in the photo-Fenton-like process (D) for BPA. In the case of TCS (Fig. 13 C and F), the catalysts synthesized using Al-PILC as catalytic support behaved in a very similar manner. Differing values were obtained for the catalyst synthesized using Mt as catalytic support for both TCS (Fig. 13 - C and F) and BPA (Fig. 13 - A and D), while for 2,6-DCP this was the case for Al-PILC$_{BE}$ (Fig. 13 - B and E). These results illustrate the relationship between pollutant and catalyst and the difference in the removal behavior of the catalysts depending on their catalytic support. The differences between those catalysts synthesized using the three Al-PILC corroborate their morphological and compositional differences, thereby highlighting the importance of the aluminum source used in their synthesis and how this affects their possible use in environmental remediation.

3.3. By-product identification

In studies related to the removal of organic compounds from water by degradation is crucial to know both the remaining concentration of the target pollutant and the composition of the sample at the end of the process. Identification of the molecules in the final sample is important because, on occasions, the by-products obtained upon pollutant degradation can be even more toxic and persistent than their parent compounds [1,4,11,50]. This information is also relevant to understand how the target pollutant is degraded and explain the degradation pathway.

The aim of the current study was not to elucidate the reactions that occur in the degradation pathway of all three organic pollutants studied nor to quantify the by-products resulting from the reaction. Instead, the by-products formed by all three target organic pollutants were tentatively identified at different stages of the reaction and the degradation pathway was proposed by considering both the by-products identified at the different reaction times analyzed and the different pathways proposed by other authors, bearing in mind the principles of organic chemistry.

For the three organic pollutants analyzed herein, we found the same by-products when using both Fenton and photo-Fenton reactions. In the case of TCS, nine products were found during the reaction: 4-

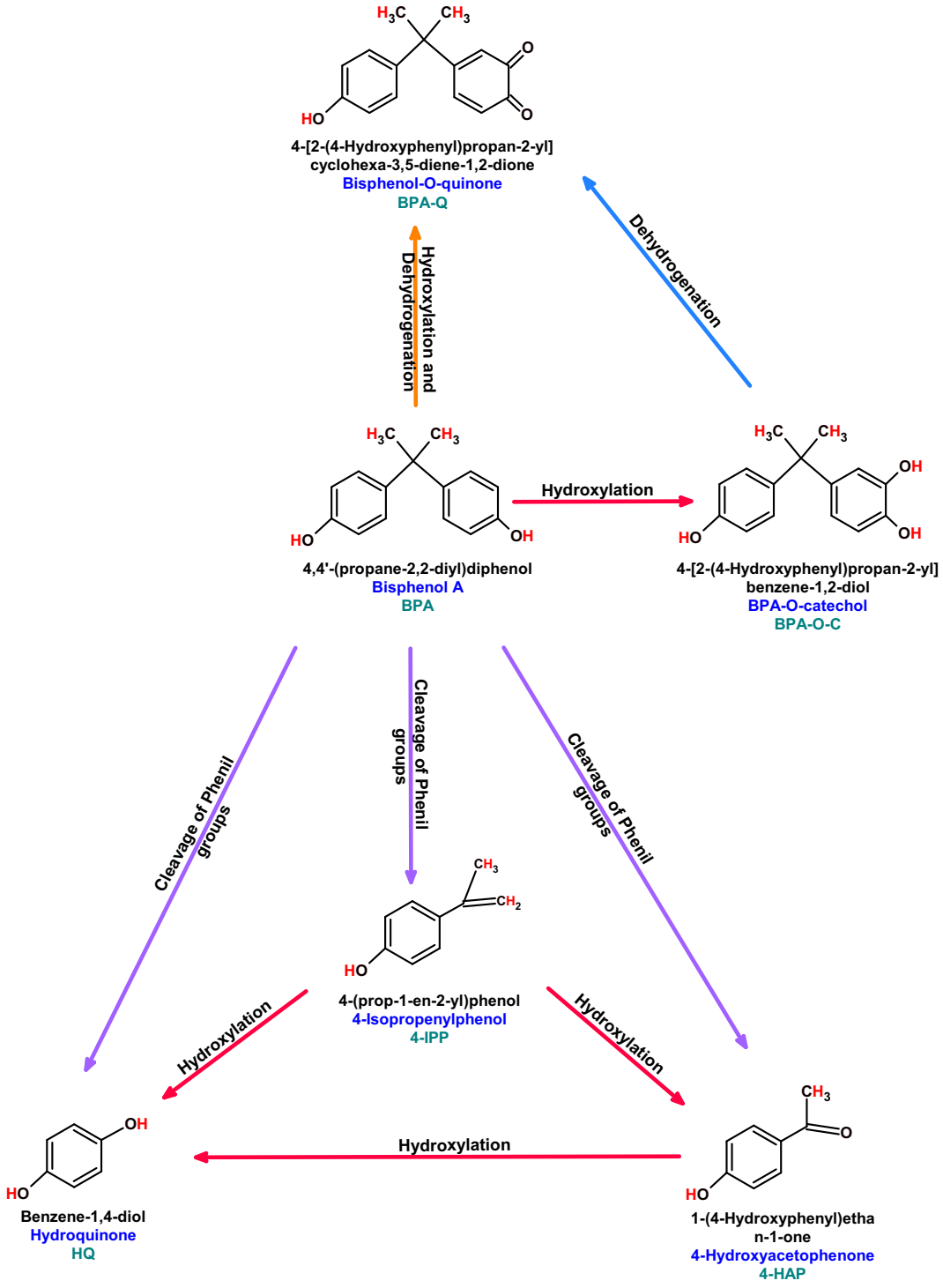

Fig. 16. Possible degradation pathway of BPA.

chlorocatehol (4-CC) 2,4-dichlorophenol (2,4-DCP), 2-chloro-5-(4-chloro-2-hydroxyphenoxy)benzene-1,4-diol (HPBD), 2-chloro-5-(2,4-dichloro-5-hydroxyphenoxy)cyclohexa-2,5-diene-1,4-dione (HPCD), 4,6-dichloro-1,2-benzenediol (4,6-DC-1,2-BD), and 4,6-dichlororesorcinol (4,6-DCR), monochlorophenol (MCP), chlorohydroquinone (CHQ), and *p*-hydroquinone of triclosan (*p*-HT). Fig. S3 shows the extracted ion chromatograms (XIC) for the main by-products identified and Table S7 the proposed structures of these by-products. The results obtained are in accordance with those published by other authors, who identified the following compounds as by-products of the oxidation of TCS: *p*-HT [8,51], 2,4-DCP [8,14,16,51–56], 4-CC [8,14,52–57], 4,6-DC-1,2-BD [8], 4,6-DCR, [8], HPCD [7]. Of these by-products, 2,4-DCP and 4-CC have also been reported as photo-products of TCS [1,6,12,15,16,52,58–61].

As mentioned previously, the aim of this work was not to quantify the by-products during the reaction but to elucidate the changes in their concentration during it. As such, 2,4-DCP was identified among the peaks in the HPLC chromatogram using a commercial reagent (Sigma Aldrich). Fig. S4 shows the region for 2,4-DCP in the HPLC chromatogram at different sampling times ranging from 15 to 240 min. This figure

reveals that the signal corresponding to 2,4-DCP changes during the experiment, increasing in intensity as the reaction proceeds. The probable pathway for the degradation of TCS in this work was proposed based on the different molecules tentatively identified and the oxidation pathways proposed by other authors such as Wang et al. [7], Apell et al. [15], Peng et al. [14], Hossein et al. [12], and Munoz et al. [8], (see Fig. 14). The structure of TCS has two positions for hydroxyl radical attack as a result of the OH group, which has a directing nature. Thus, if the radical attacks in the para-position, a hydroxylation occurs and *p*-HT is formed, whereas if the radical attacks in the ortho-position, an ether bond cleavage occurs, thereby opening one of the aromatic rings and forming 2,4-DCP and/or 4-CC; the latter can also be formed from 2,4-DCP upon hydroxylation and dechlorination. Given the compounds identified, it is likely that 2,4-DCP undergoes three different degradation reactions: dechlorination, hydroxylation, or hydroxylation plus dechlorination. Monochlorophenol (MCP) is formed by dechlorination, 4,6-DCR and 4,6-DC-1,2-BD by hydroxylation after attack of the hydroxyl radical at the meta- or ortho-position, respectively, and 4-CC and CHQ by hydroxylation and dechlorination due to substitution of the chlorine atom at the ortho- or para-position. HPCD, which was also identified among the products, can be formed from TCS or *p*-HT by hydroxylation followed by dehydrogenation in both cases. Finally, *p*-HT can be converted into HPBD by hydroxylation followed by dechlorination. The presence of triclosan dimers has also been reported as a result of a polymerization reaction that can be favored by the high concentration of chlorophenols in the presence of UV light [58]. In this work, however, no TCS dimers or any other polymerization products were found. Given the by-products formed, we propose that triclosan degradation under both our experimental conditions occurs as a result of ether bond cleavage, hydroxylation, dechlorination, hydrodechlorination, and dehydrogenation.

In the case of the degradation of 2,6-DCP, eight by-products were identified. The main by-products were 2,6-dichlorohydroquinone (2,6-DCHQ), 2,6-dichloro-*p*-benzoquinone (2,6-DCBQ), 2,6-dihydroxycyclohexa-2,5-diene-1,4-dione (2,6-DHCH-2,5-D-1,4-D), 2-hydroxy-*p*-benzoquinone (2-HBQ), and *p*-benzoquinone (BQ). The extracted ion chromatograms (XIC) of these by-products are presented in Fig. S5 and their proposed structures in Table S7. Other compounds tentatively identified during the reaction were 1,2,3,5-tetrahydroxybenzene (1,2,3,5-THB), 1,2,4-trihydroxybenzene (1,2,4-THB), chlorohydroquinone (CHQ), and a few short-chain acids. The results obtained agree with those reported by other authors, such as Dai et al. [62] and Norabadi et al. [62], who also studied the oxidative degradation of 2,6-DCP. Given both the oxidation pathways published by these authors and the products identified in this work at the sampling times used, a possible pathway for the degradation of 2,6-DCP was proposed. This tentative pathway is shown in Fig. 15. If the •OH radical attacks the benzene ring of 2,6-DCP in the para-position, a hydroxylation occurs and DCHQ is formed. CHQ, 2,6-DCBQ, and BQ can then be formed by dechlorination, dehydrogenation, or dechlorination plus dehydrogenation of 2,6-DCHQ, respectively. CHQ and 2,6-DCBQ can also be formed from 2,6-DCP by hydroxylation plus dechlorination or hydroxylation and dehydrogenation. Both hydroxylations occur in the para-position. The hydroxylation plus dechlorination of CHQ for substitution of the chlorine atom at the ortho-position gives 1,2,4-THB which, in turn, has two possible degradation reactions pathways, namely dehydrogenation or hydroxylation, that form 2-HBQ or 1,2,3,5-THB, respectively. 1,2,3,5-THB can also be obtained from 2,6-DCP by hydroxylation plus dechlorination of both chlorine atoms. Similarly, 1,2,3,5-THB can be converted into 2,6-DHCH-2,5-D-1,4-D by way of a dehydrogenation reaction.

Finally, analysis of the solutions obtained from the oxidation of BPA showed five by-products during the reaction: BPA-O-catechol (BPA-O-C), bisphenol-O-quinone (BPA-Q), 3-hydroxy-4-(2-hydroxypropan-2-yl) cyclohexa-3,5-diene-1,2-dione (3-H-4-2-HP-2-C-3,5-D-1,2-D), 4-hydroxyacetophenone (4-HAP), 4-isopropenylphenol (4-IPP), and hydroquinone (HQ). These products have been reported by other authors: BPA-O-C [63–69], BPA-Q [63,65], 4-IPP [20,64,66–68,70,71], 4-HAP [20,63,64,66–68,70], 3-H-4-2-HP-2-C-3,5-D-1,2-D [68], HQ [20,66–68,70]. Fig. S6 shows the extracted ion chromatograms (XIC) of BPA and its by-products and Table S7 their proposed structures. Based on the products identified and the pathway put forward in the studies referenced above, an alternative pathway for the degradation of BPA was proposed, as shown in Fig. 16. In light of the products formed, the •OH radical attacks BPA mainly at two positions. In the first one, the hydroxyl radical attacks the benzene ring of BPA to give BPA-O-C by way of a radical addition; BPA-O-C, in turn, forms BPA-Q by dehydrogenation. In the second one, the •OH radical attacks the other vulnerable position of BPA, namely the C—C bond between the aromatic ring and the isopropyl group in the molecule, thus resulting in cleavage of the phenyl groups of BPA and forming 4-IPP, HQ, and 4-HAP. These three compounds can also be formed from BPA-O-C by cleavage of the phenyl groups.

The oxidation of TCS, 2,6-DCP, and BPA mainly occurs due to the attack of •OH radicals. Hydroxyl radicals (•OH) are vital in the Fenton process as they are responsible for initiating sequential degradation of the organic pollutants upon reaction with them [71]. In this process, iron catalyzes the decomposition of H_2O_2 to form these hydroxyl radicals [20]. The prevalent intermediates found in this work were hydroquinones and quinones, which is in agreement with the results obtained by other authors, who have reported those compounds as the predominant intermediates in the degradation of chlorophenols in general [72,73]. Formation of the different quinones identified as by-products in this work was proposed as a result of the oxidation of hydroquinones and related compounds via a two-step successive single-electron transfer, in agreement with the principles of organic chemistry [62]. In all three cases, the aromatic compounds formed are further oxidized in subsequent steps, undergoing ring-opening reactions that result in the formation of different aliphatic compounds, such as alcohols and short-chain acids. A few such acids, including maleic and oxalic acid, were identified in the oxidation experiments for all three pollutants. Finally, all the intermediate molecules were mineralized to CO_2 and H_2O by way of decarboxylation and oxidation processes. The compounds identified in the solutions remaining at the end of the experiments showed that the toxicity of TCS, 2,6-DCP, and BPA solutions was gradually reduced as a result of oxidation via both Fenton and photo-Fenton processes.

4. Conclusions

In this study, montmorillonite (Mt) and three alumina-pillared-montmorillonites (Al-PILC$_{AE}$, Al-PILC$_{BE}$, and Al-PILC$_{CM}$) have been used as catalytic supports to synthesize Fe_2O_3/TiO_2/Mt and Fe_2O_3/TiO_2/Al-PILC catalysts. The success of the synthesis was evaluated using several techniques, such as SEM(EDX)/TEM, XRD, and N_2 adsorption experiments at −196 °C. The statistical analysis revealed the importance of the titanium/iron ratio used in the synthesis. TCS and 2,6-DCP were almost completely removed (~100 %) by both Fenton-like (240 and 420 min) and photo-Fenton-like (30 and 90 min) reactions using Fe_2O_3/TiO_2/Al-PILC as catalysts. The highest removal value for BPA was 80.14 ± 1.93 % by the photo-Fenton-like reaction (120 min). TCS showed good degradation results irrespective of the catalytic support evaluated, whereas 2,6-DCP and BPA exhibited better results when using Fe_2O_3/TiO_2/Al-PILC$_{AE}$ and Fe_2O_3/TiO_2/Al-PILC$_{BE}$. The highest removal values were achieved using the catalyst with the highest content of both titanium and iron (20 wt%) in all cases. For all three pollutants, the amount removed in the equimolar mixed-component solutions was lower than in the single-component experiments, with values up to 1.77- (TCS), 16.82- (2,6-DCP), and 1.33-times smaller (BPA).

Results highlighted the importance of the catalytic support and corroborated the differences between the three Al-PILC, thereby agreeing with their characterization. This highlights the impact of the aluminum source used in their synthesis and how it may affect their possible use in environmental remediation. Analysis of the by-products

showed nine, eight, and five main by-products for TCS, 2,6-DCP, and BPA, respectively, and the results obtained allowed us to put forward a possible degradation pathway for each pollutant. In general, our results indicate that the Fe_2O_3/TiO_2/Mt and Fe_2O_3/TiO_2/Al-PILC catalysts used in this work are suitable for removing emerging contaminants such as TCS, 2,6-DCP and BPA from water by way of both Fenton-like and photo-Fenton-like reactions.

This work has allowed the evaluation of a material synthesized from a hazardous industrial waste as a catalyst. The results have been better than those obtained when the catalyst obtained through commercial precursors is applied. This behavior can be explained from a synergistic effect produced by the metals that are extracted in the recovery process. Therefore, a possible path for the future is opened for the recovery of this type of waste, as well as others with similar characteristics. All this within the new concept of the so-called *Circular Economy*.

Research ethics

We further confirm that any aspect of the work covered in this manuscript that has involved human patients has been conducted with the ethical approval of all relevant bodies and that such approvals are acknowledged within the manuscript.

Funding

No funding was received for this work.

Declaration of competing interest

None.

Data availability

No data was used for the research described in the article.

Acknowledgments

The authors are grateful for financial support from the Spanish Ministry of Science and Innovation (MCIN/AEI/10.13039/501100011033) through project PID2020-112656RB-C21 Open access funding provided by Universidad Pública de Navarra. YC thanks the Universidad Pública de Navarra for a pre-doctoral grant (IberusTalent, European Union's H2020 research and innovation program under Marie Sklodowska-Curie grant agreement N° 801586). AG also thanks Banco Santander for funding via the Research Intensification Program.

Appendix A. Supplementary data

Supplementary data to this article can be found online at https://doi.org/10.1016/j.jwpe.2023.103494.

References

[1] L. Sanchez-Prado, M. Llompart, M. Lores, C. García-Jares, J.M. Bayona, R. Cela, Monitoring the photochemical degradation of triclosan in wastewater by UV light and sunlight using solid-phase microextraction, Chemosphere 65 (2006) 1338–1347, https://doi.org/10.1016/j.chemosphere.2006.04.025.

[2] Y. Cardona, M.A. Vicente, S.A. Korili, A. Gil, Progress and perspectives for the use of pillared clays as adsorbents for organic compounds in aqueous solution, Rev. Chem. Eng. 38 (2022), https://doi.org/10.1515/revce-2020-0015.

[3] M. Palencia, T.A. Lerma, V. Garcés, M.A. Mora, J.M. Martínez, S.L. Palencia, Chapter 21 - removal of emergent pollutants of waters, in: M. Palencia, T.A. Lerma, V. Garcés, M.A. Mora, J.M. Martínez, S.L.B.T.-E.F.P. Palencia (Eds.), Adv. Green Sustain. Chem, Elsevier, 2021, pp. 327–340, https://doi.org/10.1016/B978-0-12-821842-6.00023-3.

[4] M. Mezcua, M.J. Gómez, I. Ferrer, A. Aguera, M.D. Hernando, A.R. Fernández-Alba, Evidence of 2,7/2,8-dibenzodichloro-p-dioxin as a photodegradation product of triclosan in water and wastewater samples, Anal. Chim. Acta 524 (2004) 241–247, https://doi.org/10.1016/j.aca.2004.05.050.

[5] C. Magro, E.P. Mateus, J.M. Paz-Garcia, A.B. Ribeiro, Emerging organic contaminants in wastewater: understanding electrochemical reactors for triclosan and its by-products degradation, Chemosphere 247 (2020), 125758, https://doi.org/10.1016/j.chemosphere.2019.125758.

[6] F. Tohidi, Z. Cai, Fate and mass balance of triclosan and its degradation products: comparison of three different types of wastewater treatments and Aerobic/Anaerobic sludge digestion, J. Hazard. Mater. 323 (2017) 329–340, https://doi.org/10.1016/j.jhazmat.2016.04.034.

[7] S. Wang, Z. Chen, Z. Wang, Y. Fu, Y. Liu, Enhanced degradation of triclosan using UV–Fe2+ synergistic activation of peracetic acid, Environ. Sci. Water Res. Technol. 7 (2021) 630–637, https://doi.org/10.1039/D0EW01095B.

[8] M. Munoz, Z.M. de Pedro, J.A. Casas, J.J. Rodriguez, Triclosan breakdown by Fenton-like oxidation, Chem. Eng. J. 198–199 (2012) 275–281, https://doi.org/10.1016/j.cej.2012.05.097.

[9] N. Plattard, A. Dupuis, V. Migeot, S. Haddad, N. Venisse, An overview of the literature on emerging pollutants: chlorinated derivatives of bisphenol a (ClxBPA), Environ. Int. 153 (2021), 106547, https://doi.org/10.1016/j.envint.2021.106547.

[10] D. Krishnaiah, A. Baskaran, S.M. Anisuzzaman, D.M.Reddy Prasad, Removal of 2,6-dichlorophenol by adsorption with activated polypropylene nanofiber, J. King Saud Univ. - Eng. Sci. (2021), https://doi.org/10.1016/j.jksues.2021.10.007.

[11] R.A. Torres, C. Pétrier, E. Combet, F. Moulet, C. Pulgarin, Bisphenol a mineralization by integrated ultrasound-UV-iron (II) treatment, Environ. Sci. Technol. 41 (2007) 297–302, https://doi.org/10.1021/es061440e.

[12] H. Azarpira, M. Sadani, M. Abtahi, N. Vaezi, S. Rezaei, Z. Atafar, S.M. Mohseni, M. Sarkhosh, M. Ghaderpoori, H. Keramati, R. Hosseini Pouya, A. Akbari, V. Fanai, Photo-catalytic degradation of triclosan with UV/Iodide/ZnO process: performance, kinetic, degradation pathway, energy consumption and toxicology, J. Photochem. Photobiol. A Chem. 371 (2019) 423–432, https://doi.org/10.1016/j.jphotochem.2018.10.041.

[13] E. Norabadi, S.D. Ashrafi, H. Kamani, A. Jahantiq, Degradation of 2,6-dichlorophenol by fe-doped TiO2 sonophotocatalytic process: kinetic study, intermediate product, degradation pathway, Int. J. Environ. Anal. Chem. (2020) 1–16, https://doi.org/10.1080/03067319.2020.1837122.

[14] J. Peng, Y. Zhang, C. Zhang, D. Miao, J. Li, H. Liu, L. Wang, S. Gao, Removal of triclosan in a Fenton-like system mediated by graphene oxide: reaction kinetics and ecotoxicity evaluation, Sci. Total Environ. 673 (2019) 726–733, https://doi.org/10.1016/j.scitotenv.2019.03.354.

[15] J.N. Apell, S. Kliegman, C. Solá-Gutiérrez, K. McNeill, Linking Triclosan's structural features to its environmental fate and photoproducts, Environ. Sci. Technol. 54 (2020) 14432–14441, https://doi.org/10.1021/acs.est.0c05121.

[16] Q.-S. Li, H.-W. Cai, G.-X. Li, G.-Y. Chen, X.-Y. Ma, W.-L. He, Degradation behavior of triclosan by co-exposure to chlorine dioxide and UV irradiation: influencing factors and toxicity changes, Environ. Sci. Pollut. Res. Int. 25 (2018) 9391–9401, https://doi.org/10.1007/s11356-018-1223-z.

[17] K.H. Hama Aziz, H. Miessner, S. Mueller, A. Mahyar, D. Kalass, D. Moeller, I. Khorshid, M.A.M. Rashid, Comparative study on 2,4-dichlorophenoxyacetic acid and 2,4-dichlorophenol removal from aqueous solutions via ozonation, photocatalysis and non-thermal plasma using a planar falling film reactor, J. Hazard. Mater. 343 (2018) 107–115, https://doi.org/10.1016/j.jhazmat.2017.09.025.

[18] K.H. Hama Aziz, Application of different advanced oxidation processes for the removal of chloroacetic acids using a planar falling film reactor, Chemosphere 228 (2019) 377–383, https://doi.org/10.1016/j.chemosphere.2019.04.160.

[19] Z. Moravvej, E. Soroush, M.R. Rahimpour, in: A. Basile, K.B.T.-C.T, F.D. on (Bio-) M. Ghasemzadeh (Eds.), Chapter 9 - Achievements in Hybrid Processes for Wastewater and Water Treatment, Elsevier, 2020, pp. 239–262, https://doi.org/10.1016/B978-0-12-817378-7.00009-4.

[20] M. Wang, X. Su, S. Yang, L. Li, C. Li, F. Sun, J. Dong, Y. Rong, Bisphenol a degradation by Fenton advanced oxidation process and operation parameters optimization, E3S Web Conf. 144 (2020) 1014, https://doi.org/10.1051/e3sconf/202014401014.

[21] M. Ismael, Photo-Fenton reaction enhanced visible-light activity of p- photo-Fenton reaction enhanced visible-light activity of p-CuFe2O4/n-g-C3N4 heterojunction composites synthesized by a simple ultrasonic-assisted route for organic pollutants degradation, Mater. Res. Bull. 151 (2022), 111803, https://doi.org/10.1016/j.materresbull.2022.111803.

[22] L. Xu, J. Wang, Fenton-like degradation of 2,4-dichlorophenol using Fe3O4 magnetic nanoparticles, Appl. Catal. B Environ. 123–124 (2012) 117–126, https://doi.org/10.1016/j.apcatb.2012.04.028.

[23] A. Mishra, A. Mehta, M. Sharma, S. Basu, Enhanced heterogeneous photodegradation of VOC and dye using microwave synthesized TiO2/Clay nanocomposites: a comparison study of different type of clays, J. Alloys Compd. 694 (2017) 574–580, https://doi.org/10.1016/j.jallcom.2016.10.036.

[24] B. González-Rodríguez, R. Trujillano, V. Rives, M.A. Vicente, A. Gil, S.A. Korili, Structural, textural and acidic properties of cu-, fe- and cr-doped ti-pillared montmorillonites, Appl. Clay Sci. 118 (2015) 124–130, https://doi.org/10.1016/j.clay.2015.09.010.

[25] M.C. Dlamini, M.S. Maubane-Nkadimeng, J.A. Moma, The use of TiO2/clay heterostructures in the photocatalytic remediation of water containing organic pollutants: a review, J. Environ. Chem. Eng. 9 (2021), 106546, https://doi.org/10.1016/j.jece.2021.106546.

[26] Y. Cardona, S.A. Korili, A. Gil, Understanding the formation of Al13 and Al30 polycations to the development of microporous materials based on Al13-and Al30-PILC montmorillonites: a review, Appl. Clay Sci. 203 (2021), 105996, https://doi.org/10.1016/j.clay.2021.105996.

[27] H.Y. Zhu, J.A. Orthman, J.-Y. Li, J.-C. Zhao, G.J. Churchman, E.F. Vansant, Novel composites of TiO2 (Anatase) and silicate nanoparticles, Chem. Mater. 14 (2002) 5037–5044, https://doi.org/10.1021/cm0205884.
[28] S. Balcı, F. Tomul, Catalytic wet peroxide oxidation of phenol through mesoporous silica-pillared clays supported iron and/or titanium incorporated catalysts, J. Environ. Manag. 326 (2023), 116835, https://doi.org/10.1016/j.jenvman.2022.116835.
[29] M. Candan Karaeyvaz, S. Balci, One pot synthesis of aluminum pillared intercalated layered clay supported silicotungstic acid (STA/Al-PILC) catalysts, Microporous Mesoporous Mater. 323 (2021), 111193, https://doi.org/10.1016/j.micromeso.2021.111193.
[30] M. Asgari, G. Vitale, U. Sundararaj, Synthesis and characterization of a novel nickel pillared–clay catalyst: in-situ carbon nanotube–clay hybrid nanofiller from ni-PILC, Appl. Clay Sci. 205 (2021), 106064, https://doi.org/10.1016/j.clay.2021.106064.
[31] Z. Cheng, B. Feng, Z. Chen, J. Zheng, J. Li, S. Zuo, La2O3 modified silica-pillared clays supported PtOx nanocrystalline catalysts for catalytic combustion of benzene, Chem. Eng. J. 392 (2020), 123747, https://doi.org/10.1016/j.cej.2019.123747.
[32] Y. Cardona, A. Węgrzyn, P. Miśkowiec, S.A. Korili, A. Gil, Catalytic photodegradation of organic compounds using TiO2/Pillared clays synthesized using a nonconventional aluminum source, Chem. Eng. J. 446 (2022), 136908, https://doi.org/10.1016/j.cej.2022.136908.
[33] Y. Cardona, S.A. Korili, A. Gil, A nonconventional aluminum source in the production of alumina-pillared clays for the removal of organic pollutants by adsorption, Chem. Eng. J. 425 (2021), 130708, https://doi.org/10.1016/j.cej.2021.130708.
[34] B.A. Omran, K.-H. Baek, Valorization of agro-industrial biowaste to green nanomaterials for wastewater treatment: approaching green chemistry and circular economy principles, J. Environ. Manag. 311 (2022), 114806, https://doi.org/10.1016/j.jenvman.2022.114806.
[35] R. Djellabi, M.F. Ghorab, G. Cerrato, S. Morandi, S. Gatto, V. Oldani, A. Di Michele, C.L. Bianchi, Photoactive TiO2–Montmorillonite composite for degradation of organic dyes in water, J. Photochem. Photobiol. A Chem. 295 (2014) 57–63, https://doi.org/10.1016/j.jphotochem.2014.08.017.
[36] S. Deepracha, K. Vibulyaseak, M. Ogawa, Chapter 2.1 - complexation of TiO2 with clays and clay minerals for hierarchically designed functional hybrids, in: K. Ariga, M.B.T.-A.S.N. Aono (Eds.), Micro Nano Technol, William Andrew Publishing, 2019, pp. 125–150, https://doi.org/10.1016/B978-0-12-813341-5.00010-3.
[37] H. Ayoub, T. Roques-Carmes, O. Potier, B. Koubaissy, S. Pontvianne, A. Lenouvel, C. Guignard, E. Mousset, H. Poirot, J. Toufaily, T. Hamieh, Iron-impregnated zeolite catalyst for efficient removal of micropollutants at very low concentration from Meurthe River, Environ. Sci. Pollut. Res. Int. 25 (2018) 34950–34967, https://doi.org/10.1007/s11356-018-1214-0.
[38] L. Covinich, F. Felissia, P. Massa, R. Fenoglio, M.C. Area, Kinetic modeling of a heterogeneous Fenton-type oxidative treatment of complex industrial effluent, Int. J. Ind. Chem. 9 (2018) 215–229, https://doi.org/10.1007/s40090-018-0151-6.
[39] J. Poerschmann, U. Trommler, T. Górecki, Aromatic intermediate formation during oxidative degradation of bisphenol a by homogeneous sub-stoichiometric Fenton reaction, Chemosphere 79 (2010) 975–986, https://doi.org/10.1016/j.chemosphere.2010.03.030.
[40] A.-R.A. Giwa, I.A. Bello, A.B. Olabintan, O.S. Bello, T.A. Saleh, Kinetic and thermodynamic studies of Fenton oxidative decolorization of methylene blue, Heliyon 6 (2020), e04454, https://doi.org/10.1016/j.heliyon.2020.e04454.
[41] J. Einax, Chemometrics in Environmental Chemistry - Applications, Springer Berlin, Heidelberg, 1995, https://doi.org/10.1007/978-3-540-49150-7.
[42] A.L. Patterson, The scherrer formula for X-ray particle size determination, Phys. Rev. 56 (1939) 978–982, https://doi.org/10.1103/PhysRev.56.978.
[43] A. Abbasi, D. Ghanbari, M. Salavati-Niasari, M. Hamadanian, Photo-degradation of methylene blue: photocatalyst and magnetic investigation of Fe2O3–TiO2 nanoparticles and nanocomposites, J. Mater. Sci. Mater. Electron. 27 (2016) 4800–4809, https://doi.org/10.1007/s10854-016-4361-4.
[44] S.R. Mirmasoomi, M. Mehdipour Ghazi, M. Galedari, Photocatalytic degradation of diazinon under visible light using TiO2/Fe2O3 nanocomposite synthesized by ultrasonic-assisted impregnation method, Sep. Purif. Technol. 175 (2017) 418–427, https://doi.org/10.1016/j.seppur.2016.11.021.
[45] B. Sharma, P.K. Boruah, A. Yadav, M.R. Das, TiO2–Fe2O3 nanocomposite heterojunction for superior charge separation and the photocatalytic inactivation of pathogenic bacteria in water under direct sunlight irradiation, J. Environ. Chem. Eng. 6 (2018) 134–145, https://doi.org/10.1016/j.jece.2017.11.025.
[46] M. Thommes, K. Kaneko, A.V. Neimark, J.P. Olivier, F. Rodriguez-Reinoso, J. Rouquerol, K.S.W. Sing, Physisorption of gases, with special reference to the evaluation of surface area and pore size distribution (IUPAC technical Report), Pure Appl. Chem. 87 (2015) 1051–1069, https://doi.org/10.1515/pac-2014-1117.
[47] M.E. Hassan, Y. Chen, G. Liu, D. Zhu, J. Cai, Heterogeneous photo-Fenton degradation of methyl Orange by Fe2O3/TiO2 nanoparticles under visible light, J. Water Process Eng. 12 (2016) 52–57, https://doi.org/10.1016/j.jwpe.2016.05.014.
[48] M.J. Valero-Romero, J.G. Santaclara, L. Oar-Arteta, L. van Koppen, D.Y. Osadchii, J. Gascon, F. Kapteijn, Photocatalytic properties of TiO2 and fe-doped TiO2 prepared by metal organic framework-mediated synthesis, Chem. Eng. J. 360 (2019) 75–88, https://doi.org/10.1016/j.cej.2018.11.132.
[49] H.-E. Kim, J. Lee, H. Lee, C. Lee, Synergistic effects of TiO2 photocatalysis in combination with Fenton-like reactions on oxidation of organic compounds at circumneutral pH, Appl. Catal. B Environ. 115–116 (2012) 219–224, https://doi.org/10.1016/j.apcatb.2011.12.027.
[50] K.H. Hama Aziz, H. Miessner, S. Mueller, D. Kalass, D. Moeller, I. Khorshid, M.A. M. Rashid, Degradation of pharmaceutical diclofenac and ibuprofen in aqueous solution, a direct comparison of ozonation, photocatalysis, and non-thermal plasma, Chem. Eng. J. 313 (2017) 1033–1041, https://doi.org/10.1016/j.cej.2016.10.137.
[51] H. Zhang, C.-H. Huang, Oxidative transformation of triclosan and chlorophene by manganese oxides, Environ. Sci. Technol. 37 (2003) 2421–2430, https://doi.org/10.1021/es026190q.
[52] X. Xie, C. Chen, X. Wang, J. Li, S. Naraginti, Efficient detoxification of triclosan by a S-Ag/TiO2@g-C3N4 hybrid photocatalyst: process optimization and bio-toxicity assessment, RSC Adv. 9 (2019) 20439–20449, https://doi.org/10.1039/C9RA03279G.
[53] B. Yang, G.-G. Ying, J.-L. Zhao, L.-J. Zhang, Y.-X. Fang, L.D. Nghiem, Oxidation of triclosan by ferrate: reaction kinetics, products identification and toxicity evaluation, J. Hazard. Mater. 186 (2011) 227–235, https://doi.org/10.1016/j.jhazmat.2010.10.106.
[54] I. Sirés, N. Oturan, M.A. Oturan, R.M. Rodríguez, J.A. Garrido, E. Brillas, Electro-Fenton degradation of antimicrobials triclosan and triclocarban, Electrochim. Acta 52 (2007) 5493–5503, https://doi.org/10.1016/j.electacta.2007.03.011.
[55] T. Methatham, M.-C. Lu, C. Ratanatamskul, Effect of operating parameters on triclosan degradation by Fenton's reagents combined with an electrochemical system, Desalin. Water Treat. 52 (2014) 920–928, https://doi.org/10.1080/19443994.2013.827308.
[56] J.D. García-Espinoza, I. Robles, V. Gil, E. Becerril-Bravo, J.A. Barrios, L.A. Godínez, Electrochemical degradation of triclosan in aqueous solution. A study of the performance of an electro-Fenton reactor, J. Environ Chem. Eng. 7 (2019), 103228, https://doi.org/10.1016/j.jece.2019.103228.
[57] I. Ferrer, M. Mezcua, M.J. Gómez, E.M. Thurman, A. Agüera, M.D. Hernando, A. R. Fernández-Alba, Liquid Chromatography/Time-of-flight mass spectrometric analyses for the elucidation of the photodegradation products of triclosan in wastewater samples, Rapid Commun. Mass Spectrom. 18 (2004) 443–450, https://doi.org/10.1002/rcm.1351.
[58] Z. Chen, Q. Song, G. Cao, Y. Chen, Photolytic degradation of triclosan in the presence of surfactants, Chem. Pap. 62 (2008) 608–615, https://doi.org/10.2478/s11696-008-0077-0.
[59] S. Kliegman, S.N. Eustis, W.A. Arnold, K. McNeill, Experimental and theoretical insights into the involvement of radicals in triclosan phototransformation, Environ. Sci. Technol. 47 (2013) 6756–6763, https://doi.org/10.1021/es3041797.
[60] D.E. Latch, J.L. Packer, B.L. Stender, J. VanOverbeke, W.A. Arnold, K. McNeill, Aqueous photochemistry of triclosan: formation of 2,4-dichlorophenol, 2,8-dichlorodibenzo-p-dioxin, and oligomerization products, Environ. Toxicol. Chem. 24 (2005) 517–525, https://doi.org/10.1897/04-243r.1.
[61] J.C. Yu, T.Y. Kwong, Q. Luo, Z. Cai, Photocatalytic oxidation of triclosan, Chemosphere 65 (2006) 390–399, https://doi.org/10.1016/j.chemosphere.2006.02.011.
[62] M. Dai, Z. Luo, Y. Luo, Q. Zheng, B. Zhang, Degradation of 2,6-dichlorophenol by ferrate (VI) oxidation: kinetics, performance, and mechanism, Sep. Purif. Technol. 278 (2022), 119475, https://doi.org/10.1016/j.seppur.2021.119475.
[63] L. Xu, L. Meng, X. Zhang, X. Mei, X. Guo, W. Li, P. Wang, L. Gan, Promoting Fe3+/Fe2+ cycling under visible light by synergistic interactions between P25 and small amount of Fenton reagents, J. Hazard. Mater. 379 (2019), 120795, https://doi.org/10.1016/j.jhazmat.2019.120795.
[64] S. Sunasee, K.T. Wong, G. Lee, S. Pichiah, S. Ibrahim, C. Park, N.C. Kim, Y. Yoon, M. Jang, Titanium dioxide-based sonophotocatalytic mineralization of bisphenol a and its intermediates, Environ. Sci. Pollut. Res. 24 (2017) 15488–15499, https://doi.org/10.1007/s11356-017-9124-0.
[65] R. Frankowski, J. Płatkiewicz, E. Stanisz, T. Grześkowiak, A. Zgoła-Grześkowiak, Biodegradation and photo-Fenton degradation of bisphenol a, bisphenol S and fluconazole in water, Environ. Pollut. 289 (2021), 117947, https://doi.org/10.1016/j.envpol.2021.117947.
[66] S. Fukahori, H. Ichiura, T. Kitaoka, H. Tanaka, Capturing of bisphenol a photodecomposition intermediates by composite TiO2–Zeolite sheets, Appl. Catal. B Environ. 46 (2003) 453–462, https://doi.org/10.1016/S0926-3373(03)00270-4.
[67] S. Luo, S. Yang, C. Sun, X. Wang, Feasibility of a two-stage Reduction/Subsequent oxidation for treating tetrabromobisphenol a in aqueous solutions, Water Res. 45 (2011) 1519–1528, https://doi.org/10.1016/j.watres.2010.10.039.
[68] V. Cleveland, J.-P. Bingham, E. Kan, Heterogeneous Fenton degradation of bisphenol a by carbon nanotube-supported Fe3O4, Sep. Purif. Technol. 133 (2014) 388–395, https://doi.org/10.1016/j.seppur.2014.06.061.
[69] R.A. Torres-Palma, J.I. Nieto, E. Combet, C. Pétrier, C. Pulgarin, An innovative ultrasound, Fe2+ and TiO2 photoassisted process for bisphenol a mineralization, Water Res. 44 (2010) 2245–2252, https://doi.org/10.1016/j.watres.2009.12.050.
[70] Z. Hua, W. Ma, X. Bai, R. Feng, L. Yu, X. Zhang, Z. Dai, Heterogeneous Fenton degradation of bisphenol a catalyzed by efficient adsorptive Fe3O4/GO nanocomposites, Environ. Sci. Pollut. Res. 21 (2014) 7737–7745, https://doi.org/10.1007/s11356-014-2728-8.
[71] Y. Zhang, Z. Chen, L. Zhou, P. Wu, Y. Zhao, Y. Lai, F. Wang, Heterogeneous Fenton degradation of bisphenol a using Fe3O4@β-CD/rGO composite: synergistic effect, principle and way of degradation, Environ. Pollut. 244 (2019) 93–101, https://doi.org/10.1016/j.envpol.2018.10.028.
[72] E. Pino, M.V. Encinas, Photocatalytic degradation of chlorophenols on TiO2-325 mesh and TiO2-P25. An extended kinetic study of photodegradation under competitive conditions, J. Photochem. Photobiol. A Chem. 242 (2012) 20–27, https://doi.org/10.1016/j.jphotochem.2012.05.019.
[73] N. Venkatachalam, M. Palanichamy, V. Murugesan, Sol-gel preparation and characterization of alkaline earth metal doped Nano TiO2: efficient photocatalytic degradation of 4-chlorophenol, J. Mol. Catal. A Chem. 273 (2007) 177–185, https://doi.org/10.1016/j.molcata.2007.03.077.